

Multi-peak structure of meson spectral function in magnetic field

Haoran Li and Ziyue Wang

*School of Physics and Optoelectronic Engineering,
Beijing University of Technology, Beijing 100021, China*

(Dated: October 29, 2025)

We investigate the spectral functions of neutral and charged mesons in a hot dense medium under an external magnetic field using the two-flavor quark-meson model within the functional renormalization group (FRG) framework. Our results show that the spectral functions of σ and π_0 mesons develop new structures due to decay channels into quarks occupying different Landau levels. By consistently incorporating the momentum relations at vertices for charged particles in a magnetic field, we further show that the π_+ spectral function develops a multi-peak structure at finite temperatures, resulting from the various annihilation and decay channels available to π_+ in the magnetic environment. This multi-peak structure is further enhanced in a finite-density medium, causing the π_+ meson to become a broad resonance at lower temperatures and densities compared to neutral mesons. Such a multi-peak pattern is expected to be universal for charged mesons under magnetic fields and carries significant implications for understanding transport properties in magnetized strongly interacting fluids.

I. INTRODUCTION

Quantum Chromodynamics (QCD) phase transitions at finite temperature and density offer profound insights into the nature of strongly interacting matter, as realized in high-energy nuclear collisions and compact stars. Strong magnetic fields which can reach up to 10^{19} Gauss, ($|eB| \sim 10m_\pi^2$) in environments such as the early universe, magnetars, and non-central heavy-ion collisions [1–3] can significantly influence the behavior of QCD matter. At such intensities, QED effects become comparable in magnitude to those of QCD, leading to notable modifications in equilibrium properties. These include magnetic catalysis (MC) [4, 5], inverse magnetic catalysis (IMC) [6–8], as well as low-temperature diamagnetism [9, 10] and high-temperature paramagnetism [11–13]. Furthermore, electromagnetic fields give rise to novel non-equilibrium phenomena such as the chiral magnetic effect (CME) [14–16], underscoring the rich interplay between QCD and QED under extreme conditions.

The spectrum and dynamical properties of mesons in magnetic fields are essential for understanding both equilibrium and non-equilibrium behavior of strongly interacting matter. While meson spectrum which reflects static properties, have been widely studied through lattice simulations and model calculations [17–19], dynamical aspects such as interaction modes and transport coefficients (e.g., shear viscosity) remain relatively unexplored, despite their importance. The spectral function serves as a key probe of dynamical properties, encoding information on bound-state formation and collective excitations. Specifically, a single peak in the spectral function suggests a dominant response mode at a certain energy, whereas multiple peaks reveal distinct excitation channels at different energies or frequencies. Such structures reflect a rich internal organization, the presence of multiple energy scales, diverse interaction mechanisms, or various modes of motion in a complex system. Analyzing the positions, intensities, and shapes of these peaks is therefore crucial for uncovering the underlying microscopic physics. As will be shown in this work, the π_+ spectral function under a magnetic field at finite temperature exhibits a clear multi-peak structure. This feature not only signifies complex excitation dynamics but also carries implications for understanding transport properties in magnetized systems—such as those in heavy-ion collisions, magnetars, and the early universe.

In order to investigate the meson properties in a hot and dense medium, we adopt in this paper the quark meson model, which is widely used to study the chiral phase transition [20–22]. The beyond mean field fluctuations are included by employing the functional renormalization group (FRG) [23–26]. To calculate the spectral function in the framework of FRG, a flow equation of the two point function is required. A key aspect of our treatment concerns momentum relations at vertices under a magnetic field. Whereas momentum is generally conserved at each vertex in standard Feynman diagrams, the presence of a magnetic field significantly modifies these relations. In the absence of a magnetic field, momentum conservation arises from coordinate integration of plane waves; analogously, in a magnetic background, the momentum relation at a vertex is derived from coordinate integration of the corresponding Landau-level eigenstates. Using properly constructed vertices and diagrammatic rules, we find that the π_+ spectral function exhibits a multi-peak structure at finite temperature, resulting from annihilation and decay channels involving quarks occupying different Landau levels. The variety of these channels causes the π_+ meson to form a broad resonance at lower temperatures compared to the neutral σ and π_0 mesons.

We organize the paper as follows. The FRG flow equations for the effective potential and meson two-point functions in the quark-meson model are derived in Section II. The procedure to solve the flow equations and the numerical results including the phase diagram and meson spectral functions are shown in Section III. We summarize in Sec. IV.

The real and imaginary part of the two-point function are included in the appendix.A. We also include the threshold functions as well as the calculation details of loop diagram in magnetic field in the appendix.B and appendix.C respectively.

II. FLOW EQUATIONS

The quark-meson model is a low-energy effective theory derived from the partial bosonization of four-fermion interaction models, while preserving the global symmetries of QCD. Its two-flavor version has been widely adopted as a useful framework for investigating chiral dynamics, as it captures both the spontaneous breaking of chiral symmetry in vacuum and its restoration at finite temperature and density[20–22]. At energies below approximately 1 GeV, the relevant mesonic degrees of freedom are the pseudoscalar π and the scalar σ mesons, making this model particularly suitable for studying chiral aspects of QCD phenomenology. The Euclidean effective action of the model at finite temperature T and under external magnetic field $\vec{B} = B\hat{z}$ is given as[27]

$$\Gamma_k = \int_x \left\{ \bar{\psi} \left[\not{D} + h_k (\sigma + i\gamma_5 \vec{\tau} \vec{\pi}) \right] \psi + \frac{1}{2} (\partial_\mu \sigma)^2 + \frac{1}{2} (\partial_\mu \pi_0)^2 + \mathcal{D}_\mu \pi^+ \mathcal{D}^\mu \pi^- + U_k(\phi^2) - c\sigma \right\} \quad (1)$$

with the meson field in $O(4)$ representation $\phi = (\sigma, \vec{\pi})$. The fermionic field ψ are two flavor Dirac-spinors. $\vec{\tau}$ are the Pauli matrices in isospin space, the abbreviation stands for $\int_x = \int_0^{1/T} dx_0 \int d^3x$. For this moment we neglect the scale dependence of Yukawa coupling and wave function renormalization, namely they are kept to be constant $Z = 1$ (local potential approximation), and $h = 3.2$ to fit the quark mass in vacuum. The explicit chiral symmetry breaking term $-c\sigma$ corresponds to a finite current quark mass. The interaction between external magnetic field and quark field is implemented through the covariant derivative

$$\not{D} = \gamma^\mu D_\mu, \quad D_\mu = \partial_\mu - iQA_\mu, \quad Q = \text{diag}(+2e/3, -e/3). \quad (2)$$

The interaction of charged pion with the magnetic field is included by minimum coupling $\mathcal{D}_\mu = \partial_\mu - ieA_\mu$, with Landau gauge $A = -By\delta_1^k$.

A. Flow equations of effective potential

Quantum and thermal fluctuation are of particular importance in the vicinity of phase transitions and are conveniently included within the framework of the functional renormalization group(FRG). The core quantity in this approach is the averaged effective action Γ_k at the RG scale k in Euclidean space, its scale dependence is described by the flow equation [24]

$$\partial_k \Gamma_k = \text{Tr} \int_p \left[\frac{1}{2} G_{\phi,k}(p) \partial_k R_{\phi,k}(p) - G_{\psi,k}(p) \partial_k R_{\psi,k}(p) \right]. \quad (3)$$

The flow equation (3) has the form of a one loop diagram. $G_{\phi,k} = (\Gamma_k^{(2)}[\phi] + R_{\phi,k})^{-1}$ and $G_{\psi,k} = (\Gamma_k^{(2)}[\psi] + R_{\psi,k})^{-1}$ are the FRG modified meson and quark propagator. $\Gamma_k^{(2)}[\phi] = \delta^2 \Gamma_k / \delta \phi^2$ is second functional derivative with respect to bosonic field, and $\Gamma_k^{(2)}[\psi] = \delta^2 \Gamma_k / \delta \psi \delta \bar{\psi}$ corresponds to fermionic field. The symbol Tr represents the summation over all inner degrees of freedom of mesons and quarks. The flow of Γ_k from UV to IR is controlled by the cutoff functions R_k . In order to suit the finite temperature and magnetic field background setting, we adopt an anisotropic regulator depending only on p_3 throughout this work [28, 29], in the following we call it p_3 -regulator. The bosonic and fermionic regulators are chosen to be

$$\begin{aligned} R_{\phi,k} &= p_3^2 r_B(y), \\ R_{\psi,k} &= \gamma_3 p_3 r_F(y) \end{aligned} \quad (4)$$

in momentum space, with $y = p_3^2/k^2$ and $r_B(y) = (1/y - 1)\Theta(1 - y)$ and $r_F(y) = (1/\sqrt{y} - 1)\Theta(1 - y)$. The regulators $R_{\phi,k}$ and $R_{\psi,k}$ in the propagators G_ϕ and G_ψ amount to having regularized three-momenta $\tilde{p}_3^2 = \mathbf{p}^2(1 + r_B(y))$ and $\tilde{p}_3 = \mathbf{p}(1 + r_F(y))$ for bosons and fermions respectively.

For the propagators π^\pm and quarks in magnetic field, we take Landau-level representation [30, 31]. The propagators in coordinate space can be written as the Fourier transformation of the momentum space propagators,

$$G_{\pi^c, f}(r, r') = e^{i\vec{\Phi}(r_\perp, r'_\perp)} \int \frac{d^4p}{(2\pi)^4} e^{-ip \cdot (r - r')} G_{\pi^c, f}(p), \quad (5)$$

the subscript $\pi^c = \pi^\pm$ for charged pion and $f = u, d$ for quarks. $\Phi(\mathbf{r}_\perp, \mathbf{r}'_\perp)$ is the Schwinger phase defined by $\Phi(\mathbf{r}_\perp, \mathbf{r}'_\perp) = -\frac{s_\perp(x-x')(y+y')|qB|}{2}$, where $s_\perp = \text{sign}(qB)$, q is the charge of the charged complex scalar field or the fermion field. $G_{\pi^c, f}(p)$ is the corresponding propagators in momentum space. For charged complex scalar field,

$$G_{\pi^c}(p) = 2ie^{-p_\perp^2 l^2} \sum_{n=0}^{\infty} \frac{(-)^n L_n(2p_\perp^2 l^2)}{p_0^2 - (2n+1)|eB| - (p^3)^2 - m^2}, \quad (6)$$

where L_n is the Laguerre polynomial, and $p_\perp^2 = p_x^2 + p_y^2$, $l^2 = 1/|eB|$. For quarks,

$$G_f(p) = ie^{-p_\perp^2 l_f^2} \sum_{n=0}^{\infty} (-1)^n \frac{D_{f,n}(p)}{(p_0 + \mu)^2 - p_3^2 - 2n|q_f B| - m^2},$$

$$D_{f,n}(p) = 2[(p_0 + \mu)\gamma^0 - p^3\gamma^3 + m][\mathcal{P}_+ L_n(2p_\perp^2 l_f^2) - \mathcal{P}_- L_{n-1}(2p_\perp^2 l_f^2)] + 4\vec{\gamma}_\perp \cdot \vec{p}_\perp L_{n-1}^1(2p_\perp^2 l_f^2), \quad (7)$$

where $\mathcal{P}_\pm = \frac{1}{2}[1 \pm i\gamma^1\gamma^2 s_\perp^f]$ is the projector. For u-quark $s_\perp^u = +1$, $l_u^2 = \frac{3}{2}l^2$, and for d-quark $s_\perp^d = -1$, $l_d^2 = 3l^2$.

The flow equation of the effective potential is

$$\partial_k U_k = \frac{1}{2}I_\sigma^{(1)} + \frac{1}{2}I_{\pi^0}^{(1)} + \frac{1}{2}\tilde{I}_{\pi^+}^{(1)} + \frac{1}{2}\tilde{I}_{\pi^-}^{(1)} - N_c \sum_{f=u,d} I_f^{(1)}, \quad (8)$$

where $I_\phi^{(1)} = \frac{k^2}{\pi^2} \int_0^\infty p_\perp dp_\perp I_\phi^{(1)T}(E_\phi)$, $\tilde{I}_\phi^{(1)} = \frac{k^2|eB|}{\pi^2} \sum_{n=0}^\infty I_\phi^{(1)T}(E_\phi)$ and $I_f^{(1)} = \frac{k^2|q_f B|}{\pi^2} \sum_{n=0}^\infty \alpha_n I_f^{(1)T}(E_f)$ are the loop functions encoding the momentum integral and Matsubara sum in the neutral meson loop, charged pion loop, and quark loop respectively, $\alpha_n = 1$ for $n = 0$, and $\alpha_n = 2$ for $n \geq 1$. $I_\phi^{(1)T}(E_\phi)$ and $I_f^{(1)T}(E_f)$ are the threshold function encoding Matsubara sum, they presented in Appendix B. The scale-dependent effective potential U_k is a function of the invariant $\rho = \phi^2 = \sigma^2 + \vec{\pi}^2$. The curvature mass of the mesons and the quark mass are determined from

$$m_\pi^2 = 2U', \quad m_\sigma^2 = 2U' + 4\rho U'', \quad m_q^2 = h^2 \rho, \quad (9)$$

where the derivatives are $U' = \partial_\rho U$ and $U'' = \partial_\rho^2 U$, the curvature at the minimum of the effective potential yield the squared curvature masses of the pion and sigma meson. The energy of neutral meson, charged meson and quark are given correspondingly

$$E_\phi = \sqrt{k^2 + p_\perp^2 + m_\phi^2}, \quad E_{\pi^\pm} = \sqrt{k^2 + (2n+1)|eB| + m_\pi^2}, \quad E_f = \sqrt{k^2 + 2n|q_f B| + m_q^2}, \quad (10)$$

where p_\perp is the perpendicular momentum, n is the Landau level of π^\pm and quark. When turning off the magnetic field, one can simply replacing $(2n+1)|eB| \rightarrow p_\perp^2$ and $2n|q_f B| \rightarrow p_\perp^2$ in corresponding energy of π^\pm and quark. The threshold function will return to those without magnetic field by taking the replacement $|eB| \sum_{n=0}^\infty \rightarrow \int p_\perp dp_\perp$ in $\tilde{I}_{\pi^\pm}^{(1)}$ and $|q_f B| \sum_{n=0}^\infty \alpha_n \rightarrow 2 \int p_\perp dp_\perp$ in $I_f^{(1)}$.

B. Flow equation of 2-point function

We now consider the flow equations for meson two-point functions. From the flow equation for the effective action, we get only the statical properties of the mesons, namely the curvature masses defined through the effective potential. However, the thermal medium and magnetic field have much more complicated effects on the dynamical properties of mesons. From the two-point functions, one can extract the spectral functions which contain the information on full pole masses and decay properties of the mesons. In the following we consider the flow equations for two-point functions $\Gamma_{k,p}^{(2)}[\phi]$ at vanishing external momentum $\mathbf{p} = 0$ for neutral mesons and lowest Landau level for π^\pm .

The flow equation of two-point function is derived from the flow equation for the effective action Γ_k by taking second order functional derivative with respect to ϕ_i and ϕ_i^\dagger ,

$$\partial_k \Gamma_{k,p}^{(2)}[\phi_i] = \tilde{\partial}_k \text{Tr} \int_q \left[\frac{1}{2} G_{\phi,k}(q) \Gamma_k^{(4)}[\phi, \phi_i] - \frac{1}{2} G_{\phi,k}(q) \Gamma_k^{(3)}[\phi, \phi_i] G_{\phi,k}(q+p) \Gamma_k^{(3)}[\phi, \phi_i] \right. \\ \left. + G_{\psi,k}(q) \Gamma_k^{(3)}[\psi, \phi_i] G_{\psi,k}(q+p) \Gamma_k^{(3)}[\psi, \phi_i] \right], \quad (11)$$

where the symbol $\tilde{\partial}_k$ means the derivative only on the regulators R_k . It is worth emphasizing that in the above expression, the conservation of momentum is taken as an underlying assumption. However, in the background magnetic

field, the translation invariance no longer exists, neither the conservation of momentum. The evaluation of the above flow equation hence need to be started from the coordinate space.

From the definition $\Gamma^{(3)}[\phi, \phi_i] = \delta\Gamma^{(2)}[\phi]/\delta\phi_i$, $\Gamma^{(3)}[\psi, \phi_i] = \delta\Gamma^{(2)}[\psi]/\delta\phi_i$ and $\Gamma^{(4)}[\phi, \phi_i] = \delta^2\Gamma^{(2)}[\phi]/\delta\phi_i^2$ with ϕ_i the external field, we have the coupling matrices. The matrix elements are defined by $\Gamma_{ijm}^{(3)} = \partial^3\Gamma_k/\partial\phi_i\partial\phi_j\partial\phi_m$ and $\Gamma_{ijmnn}^{(4)} = \partial^4\Gamma_k/\partial\phi_i\partial\phi_j\partial\phi_m\partial\phi_n$. The non-zero matrix components are $\Gamma_{\sigma\sigma\sigma}^{(3)} = 12\sigma_k U_k'' + 8\sigma_k^3 U_k^{(3)}$, $\Gamma_{\sigma\pi\pi}^{(3)} = 4\sigma_k U_k''$, $\Gamma_{\sigma\sigma\sigma\sigma}^{(4)} = 12U_k'' + 48\sigma_k^2 U_k^{(3)} + 16\sigma_k^4 U_k^{(4)}$, $\Gamma_{\sigma\sigma\pi\pi}^{(4)} = 4U_k'' + 8\sigma_k^2 U_k^{(3)}$, $\Gamma_{\pi_0\pi_0\pi_0\pi_0}^{(4)} = 12U_k''$, $\Gamma_{\pi_+\pi_-\pi_+\pi_-}^{(4)} = 8U_k''$, $\Gamma_{\pi_+\pi_-\pi_0\pi_0}^{(4)} = 4U_k''$. The derivatives are $U' = \delta U/\delta\rho$, $U'' = \delta^2 U/\delta\rho^2$, $U^n = \delta^n U/\delta\rho^n$, and σ_k is the sigma condensate at certain scale k . The vertex related to quarks are $\Gamma_{\psi\sigma\psi}^{(3)} = g \times \mathbf{1}_D \times \mathbf{1}_f$, $\Gamma_{\psi\pi_+\psi}^{(3)} = ig\gamma_5\sigma_+$, $\Gamma_{\psi\pi_-\psi}^{(3)} = ig\gamma_5\sigma_-$, $\Gamma_{\psi\pi_0\psi}^{(3)} = ig\gamma_5\sigma_3$.

The loops in σ and π^0 two-point function are relatively simple, with the external field neutral, the loops are constructed by particles with equal but opposite charges, hence the Schwinger phase in the propagators can cancel out. In the following we present the flow equations for the pion and sigma meson 2-point functions in the external magnetic field

$$\begin{aligned} \partial_k \Gamma_{k,p_0}^{(2)}[\sigma] &= (\Gamma_{\sigma\sigma\sigma}^{(3)})^2 J_{\sigma\sigma}(p_0) + (\Gamma_{\sigma\pi\pi}^{(3)})^2 \left(J_{\pi_0\pi_0}(p_0) + \tilde{J}_{\pi_+\pi_+}(p_0) + \tilde{J}_{\pi_-\pi_-}(p_0) \right) \\ &\quad - \frac{1}{2} \Gamma_{\sigma\sigma\sigma\sigma}^{(4)} I_{\sigma}^{(2)} - \frac{1}{2} \Gamma_{\sigma\sigma\pi\pi}^{(4)} (I_{\pi_0}^{(2)} + \tilde{I}_{\pi_+}^{(2)} + \tilde{I}_{\pi_-}^{(2)}) \\ &\quad + 2g^2 N_c (J_{uu}^{\sigma}(p_0, \mu) + J_{dd}^{\sigma}(p_0, \mu)), \\ \partial_k \Gamma_{k,p_0}^{(2)}[\pi^0] &= (\Gamma_{\sigma\pi\pi}^{(3)})^2 \left(J_{\sigma\pi_0}(p_0) + J_{\pi_0\sigma}(p_0) \right) \\ &\quad - \frac{1}{2} \Gamma_{\sigma\sigma\pi\pi}^{(4)} I_{\sigma}^{(2)} - \frac{1}{2} \Gamma_{\pi\pi\pi\pi}^{(4)} I_{\pi_0}^{(2)} - \frac{1}{2} \Gamma_{\pi\pi\tilde{\pi}\tilde{\pi}}^{(4)} (\tilde{I}_{\pi_+}^{(2)} + \tilde{I}_{\pi_-}^{(2)}) \\ &\quad + 2g^2 N_c (J_{uu}^{\pi_0}(p_0, \mu) + J_{dd}^{\pi_0}(p_0, \mu)). \end{aligned} \quad (12)$$

In this formalism, the loop functions are defined as follows. $J_{\alpha\alpha}(p_0) = \frac{k^2}{\pi^2} \int_0^\infty q_\perp dq_\perp J_{\alpha\alpha}^T$ and $J_{\alpha\beta}(p_0) = \frac{k^2}{\pi^2} \int_0^\infty q_\perp dq_\perp J_{\alpha\beta}^T$ represent loop integrals with three-line vertices, where the former involves identical neutral mesons and the latter different neutral mesons. For charged mesons, the corresponding loop function is given by $\tilde{J}_{\alpha\alpha}(p_0) = \frac{k^2 |eB|}{\pi^2} \sum_{l=0}^\infty J_{\alpha\alpha}^T$ which incorporates summation over Landau levels. Similarly, $I_\phi^{(2)} = \frac{k^2}{\pi^2} \int_0^\infty q_\perp dq_\perp I_\phi^{(2)T}$ and $\tilde{I}_\phi^{(2)} = \frac{k^2 |eB|}{\pi^2} \sum_{l=0}^\infty I_\phi^{(2)T}$ denote loop functions with four-line vertices for neutral and charged mesons, respectively.

For quark loops, the function $J_{ff}^\phi(p_0, \mu) = \frac{k^2 |q_f B|}{\pi^2} \sum_n^\infty \alpha_n J_{ff}^{\phi T}(p_0, \mu)$ is introduced, where $f = u, d$ labels the quark flavor and $\phi = \sigma, \pi^0$ indicates the external meson line. The Matsubara summation, which are encapsulated in the threshold functions $J_{\alpha\alpha}^T, J_{\alpha\beta}^T, I_\phi^{(2)T}$ and $J_{ff}^{\phi T}$, are presented in Appendix B.

In order to investigate the medium effect on the meson mass and decay properties, we focus on spectral function in the particle rest frame, with vanishing spatial momentum $\vec{p} = 0$. However, for charged pion in the external magnetic field, this conventional approach is not directly applicable due to the zero-point energy associated with Landau levels. Instead, we consider the ground Landau level $n = 0$ with longitudinal momentum $p_3 = 0$ for the external line. The absence of translational invariance in charged particle propagators under a magnetic field requires that loop calculations be performed directly in coordinate space. Specifically, the flow equation for the two-point function of π_\pm includes loops formed by π_\pm and σ mesons, as well as quark loops involving u - and d -quarks—all of which carry different electric charges. In such configurations, the Schwinger phase does not cancel, and standard momentum conservation at vertices is modified. Consequently, these loops must be evaluated starting from their coordinate-space representation. For a general external π_\pm line in Landau level n with momentum components p_0 and p_3 , the corresponding eigenstate is given by $\phi_{np}(r) = \langle r|np \rangle = e^{-ip_0 t + ip_3 z} \Psi_{np_1}(\vec{r}_\perp)$, which remains a plane wave along the t - and z -directions, while in the transverse plane it is described by a Landau-level wave function. Explicitly,

$$\phi_{np}(r) = e^{-ip_0 t + ip_3 z} \frac{e^{-\frac{(y + s_\perp p_1 t)^2}{2}}}{\sqrt{2^n n! \sqrt{\pi} l}} H_n \left(\frac{y}{l} + s_\perp p_1 t \right) e^{ip_1 x}, \quad (13)$$

where $l = 1/\sqrt{qB}$ is the magnetic length, and $l = 1/\sqrt{eB}$ for π_\pm . A meson loop composed by σ and π_+ with two three-line vertex is calculated starting from a coordinate space loop

$$\text{M-Loop} = (\Gamma_{\sigma\pi\pi}^{(3)})^2 \int_{r,r'} \phi_{np}(r') G_{\pi_+}(r, r') G_\sigma(r', r) \phi_{np}^*(r). \quad (14)$$

Likewise, we also need to evaluate the quark loop constructed by u quark and d quark starting from the coordinate space. The quark propagator in the coordinate space can also be obtained by Fourier transformation (5) from the

momentum space propagator (7). The quark loop in coordinate space reads

$$\text{F-loop} = \int_{r,r'} \text{Tr} \left[\phi_{np}(r') (\sqrt{2}ig\gamma_5) G_u(r, r') (\sqrt{2}ig\gamma_5) G_d(r', r) \phi_{np}^*(r) \right]. \quad (15)$$

The detailed calculation of the M-loop and F-loop are contained in the Appendix C. After complicated calculation of integrating out the coordinate and momentum, as well as considering the FRG modification to the loop and taking the derivative to the RG-scale, we finally arrive at the flow equation of the π^+ two point function,

$$\begin{aligned} \partial_k \Gamma_{\pi^+, k}^{(2)} &= (\Gamma_{\sigma\pi\pi}^{(3)})^2 \left(\bar{J}_{\sigma\pi_c}(p_0) + \bar{J}_{\pi_c\sigma}(p_0) \right) \\ &\quad - \frac{1}{2} \Gamma_{\sigma\sigma\pi\pi}^{(4)} I_\sigma^{(2)} - \frac{1}{2} \Gamma_{\pi\pi\bar{\pi}\bar{\pi}}^{(4)} I_{\pi_0}^{(2)} - \frac{1}{2} \Gamma_{+-+-}^{(4)} (\tilde{I}_{\pi_+}^{(2)} + \tilde{I}_{\pi_-}^{(2)}) \\ &\quad + 2g^2 N_c \left(J_{du}^{\pi^+}(p_0, \mu) + J_{ud}^{\pi^+}(-p_0, \mu) \right), \end{aligned} \quad (16)$$

where $\bar{J}_{\sigma\pi_c}(p_0)$ is the loop function of a loop with three-line vertex composed by σ and π^+ . It is defined by

$$\bar{J}_{\sigma\pi_c}(p_0) = \frac{k^2}{\pi^2} \sum_{m=0}^{\infty} \int q_\perp dq_\perp \frac{1}{m!} \left(\frac{q_\perp^2}{2|eB|} \right)^m e^{-\frac{q_\perp^2}{2|eB|}} J_{\sigma\pi_c}^T(p_0), \quad (17)$$

where $J_{\sigma\pi_c}^T(p_0)$ encodes the Matsubara sum, which is defined in Appendix B. Energy of σ meson and π^+ meson are given by (10). $J_{du}^{\pi^+}(p_0, \mu)$ and $J_{ud}^{\pi^+}(-p_0, \mu)$ are the loop function of a quark loop composed by u and d quark,

$$\begin{aligned} J_{du}^{\pi^+}(p_0, \mu) &= -\frac{2k^2|eB|}{3\pi^2} \sum_{n,m=0}^{\infty} \left\{ Y_1 J_{du, mn}^{(0)T}(p_0, \mu) + \left(4m|q_d B|Y_1 - \frac{16}{3}|eB|Y_2 \right) J_{du, mn}^{(1)T}(p_0, \mu) \right\}, \\ J_{ud}^{\pi^+}(p_0, \mu) &= -\frac{2k^2|eB|}{3\pi^2} \sum_{n,m=0}^{\infty} \left\{ Y_1 J_{ud, nm}^{(0)T}(p_0, \mu) + \left(4n|q_u B|Y_1 - \frac{16}{3}|eB|Y_2 \right) J_{ud, nm}^{(1)T}(p_0, \mu) \right\}. \end{aligned} \quad (18)$$

$J_{du, mn}^{(0)T}$, $J_{du, mn}^{(1)T}$ and $J_{ud, nm}^{(0)T}$, $J_{ud, nm}^{(1)T}$ encodes the Matsubara sum in the loop, where m is the Landau level in the propagator of d-quark, and n is the Landau level in the propagator of u-quark. The details of threshold functions are included in the appendix.B. The function Y_1 and Y_2 encodes information in perpendicular momentum integral,

$$\begin{aligned} Y_1(m, n) &\equiv \frac{(-1)^m}{5^{n+1}} \int du e^{-\frac{3}{5}u} \left[L_n\left(-\frac{2}{5}u\right) L_{m-1}(u) - 5L_{n-1}\left(-\frac{2}{5}u\right) L_m(u) \right] = -\frac{2^{m-1}}{3^{n+m}} \frac{(2n+m)\Gamma(n+m)}{\Gamma(1+n)\Gamma(1+m)}, \\ Y_2(m, n) &\equiv \frac{(-1)^m}{5^{n+1}} \int du e^{-\frac{3}{5}u} u L_{n-1}^1\left(-\frac{2}{5}u\right) L_{m-1}^1(u) = -\frac{2^{m-1}}{3^{n+m}} \frac{\Gamma(n+m)}{\Gamma(n)\Gamma(m)}. \end{aligned} \quad (19)$$

These integrals are performed using

$$\int_0^{+\infty} e^{-bx} x^\alpha L_n^\alpha(\lambda x) L_m^\alpha(\mu x) dx = \frac{\Gamma(m+n+\alpha+1)}{m!n!} \frac{(b-\lambda)^n (b-\mu)^m}{b^{m+n+\alpha+1}} F[-m, -n; -m-n-\alpha, \frac{b(b-\lambda-\mu)}{(b-\lambda)(b-\mu)}], \quad (20)$$

where F is the hypergeometric function. In deriving the quark propagator, the condition $L_{-1}(x) = 0$ is assumed. As a result, the analytic expression for $Y_1(m, n)$ is valid when $m > 0$ or $n > 0$, while $Y_1(0, 0) = 0$. Similarly, the definition of $Y_2(m, n)$ implies that it is nonzero only when $m \geq 1$ and $n \geq 1$. Consequently, the quark loop contribution in the flow equation vanishes when both quarks in the propagators occupy the lowest Landau level, but becomes nonvanishing for any other combination of Landau levels. Physically, this is because a spin-0 π_+ meson cannot decay into a pair of $u\bar{d}$ -quarks both at ground Landau level whose spins are parallel to the magnetic field. The functions Y_1 and Y_2 exhibit a structure reminiscent of a binomial distribution. Specifically, for a d-quark in the m -th Landau level and a u-quark in the n -th Landau level, the amplitude is weighted by a factor proportional to $\frac{(n+m-1)!}{(n-1)!m!} \left(\frac{2}{3}\right)^m \left(\frac{1}{3}\right)^{n-1}$. This specific relation between momentum and Landau levels at the π_+ -quark vertices gives rise to diverse annihilation channels for π_+ in a thermal medium. As will be shown in the following section, these channels are responsible for the multi-peak structure observed in the π_+ spectral function at finite temperature.

In order to obtain the two-point functions in Minkowski space, we perform the analytic continuation

$$\Gamma_{k, \omega}^{(2)}[\phi_i] = \lim_{\epsilon \rightarrow 0} \lim_{p_0 \rightarrow -i(\omega+i\epsilon)} \Gamma_{k, p_0}^{(2)}[\phi_i]. \quad (21)$$

This substitution of the discrete Euclidean frequency p_0 by the continuous energy ω is done explicitly before the integration of the RG scale k . Finally, the meson spectral functions are expressed in terms of the imaginary and real parts of the retarded propagator,

$$\rho_{k,\omega}[\phi_i] = -\frac{1}{\pi} \frac{\text{Im}\Gamma_{k,\omega}^{(2)}[\phi_i]}{\left[\text{Re}\Gamma_{k,\omega}^{(2)}[\phi_i]\right]^2 + \left[\text{Im}\Gamma_{k,\omega}^{(2)}[\phi_i]\right]^2}. \quad (22)$$

III. NUMERICAL PROCESS AND RESULTS

In order to investigate spectral function at finite temperature and density, we use both Taylor expansion method [32, 33] and the grid method [34] to solve the flow equation (8). In the Taylor expansion method, the flow equation of the effective potential (8) is solved around a fixed expansion point,

$$U_k(\rho) = \sum_{n=0}^{n_{\max}} \frac{\lambda_{n,k}}{n!} (\rho - \rho_0)^n, \quad (23)$$

where ρ_0 is the expansion point, which is located at the minimum of the effective potential at $k = 0$. The maximum expansion order is chosen to be $n_{\max} = 5$. However, since the Taylor expansion method may not fully capture the behavior across first-order phase transitions, we also employ the grid method to ensure a more complete description. In the grid method, the field space of ρ is discretized into 200 points ranging from 0 to $\rho_{\max} = 200^2 \text{MeV}^2$. During the process of integrating the flow equations from the ultraviolet limit to the infrared limit, the condensates is obtained by locating the minimum of the k -dependent effective potential U_k .

In contrast to the conventional 3-momentum \vec{p} -regulator, the p_3 -regulator adopted in this work (4) selectively suppresses fluctuations only along the z -direction. This choice leads to distinct behavior in numerical computations: the renormalization group flow saturates at even lower values of k , requiring the evolution to be carried down to a sufficiently small infrared scale. Moreover, the effective potential develops enhanced concavity in the small- ρ region, where U'' becomes negative, potentially resulting in a negative squared sigma mass, $m_\sigma^2 = 2U' + 4\rho U''$. This can hinder further integration of the flow equations. To address this issue, we have implemented two alternative approaches. Method A: Whenever m_σ^2 turns negative, it is manually set to zero in the small- ρ region to allow continued flow evolution. Method B: If m_σ^2 becomes negative within an interval $[0, \rho_i]$ at some RG scale k_i , the field domain is restricted to $[\rho_i, \rho_{\max}]$ for all subsequent evolution steps. We have verified that the Taylor expansion method and both grid methods (A and B) yield consistent results in regions sufficiently far from the critical endpoint. However, very close to the critical endpoint, the Taylor expansion method becomes unreliable. In this regime, grid method B remains applicable, while grid method A proves robust across the entire phase diagram.

The numerical solution of the flow equations for the effective potential and the two-point functions requires specification of the model parameters and initial conditions. In the ultraviolet regime, the initial effective potential is chosen as

$$U_\Lambda = \frac{1}{2} m_\Lambda^2 \rho + \frac{1}{4} \lambda_\Lambda \rho^2. \quad (24)$$

The parameters m_Λ^2 , λ_Λ , and the scale-independent parameter c are determined by matching the infrared behavior at $k = 0$ to the physical meson and quark masses in vacuum. Using the input values $m_q = 300$ MeV, pion mass $m_\pi = 137$ MeV and pion decay constant $f_\pi = 93$ MeV, the corresponding initial parameters are fixed as $m_\Lambda^2/\Lambda^2 = 1.44$, $\lambda_\Lambda = 15.94$ and $c/\Lambda^3 = 0.00175$ in Taylor expansion method, and $m_\Lambda^2/\Lambda^2 = 1.56$, $\lambda_\Lambda = 18.4$ and $c/\Lambda^3 = 0.00175$ in the grid method, with the cutoff scale set to $\Lambda = 1$ GeV. For numerical evaluation, the transverse momentum integration is performed over the range $[0, p_T^{\max}]$ with $p_T^{\max} = 5$ GeV, and the summation over Landau levels is truncated at an energy upper limit of 5 GeV.

For solving the meson two-point functions, we take

$$\begin{aligned} \Gamma_{\Lambda,\omega}^{(2)}[\sigma] &= -\omega^2 + 2U'_\Lambda + 4\rho U''_\Lambda, \\ \Gamma_{\Lambda,\omega}^{(2)}[\pi_0] &= -\omega^2 + 2U'_\Lambda, \\ \Gamma_{\Lambda,\omega}^{(2)}[\pi_+] &= -\omega^2 + |eB| + 2U'_\Lambda \end{aligned} \quad (25)$$

as the initial condition. We keep a small imaginary part $\epsilon = 1$ MeV of the momentum during the calculation of the spectral function.

A. Phase diagram and screening masses

We begin with a brief overview of the phase diagram, which provides essential input for the subsequent calculation of two-point correlation functions. As shown in Fig.1, the phase structure agrees with typical predictions of the quark-meson model. Consistent with Ref.[28], the model exhibits magnetic catalysis: chiral symmetry restoration shifts to higher temperatures as the magnetic field strengthens. Moreover, the first-order phase transition becomes more pronounced with increasing magnetic field, extending to lower chemical potentials and persisting up to higher temperatures. As a result, the critical endpoint (CEP) moves toward higher temperatures with increasing magnetic field strength. The CEP locations are $(T, \mu) = (25, 274)\text{MeV}$, $(56, 272)\text{MeV}$ and $(79, 278)\text{MeV}$ for $eB = 10, 20, 30m_\pi^2$, respectively.

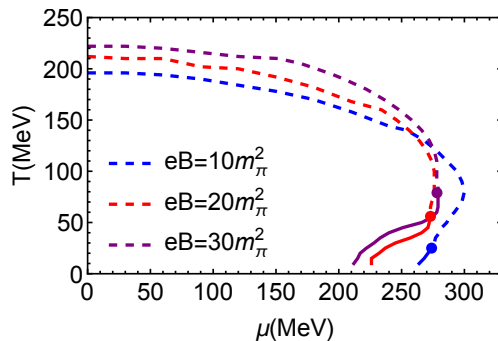


FIG. 1: Phase boundaries in the $T - \mu$ plane under different magnetic fields. Dashed lines denote crossovers; solid lines indicate first-order transitions, circles mark the critical endpoints.

In what follows, we are going to present spectral functions at various temperatures for $eB = 10 m_\pi^2$, as this magnetic field strength allows numerous annihilation and decay channels to appear within the relevant energy range. We also analyze spectral functions at different chemical potentials along a vertical line in the phase diagram crossing the CEP. For $eB = 20 m_\pi^2$, the critical temperature $T_c = 56$ MeV is high enough for thermal effects to manifest in the spectral functions. Although larger magnetic fields further increase T_c , the corresponding decay channels open at energies beyond the region of interest. Therefore, it is useful to examine the temperature and chemical potential dependence of meson screening masses, which help identify thresholds in the spectral functions.

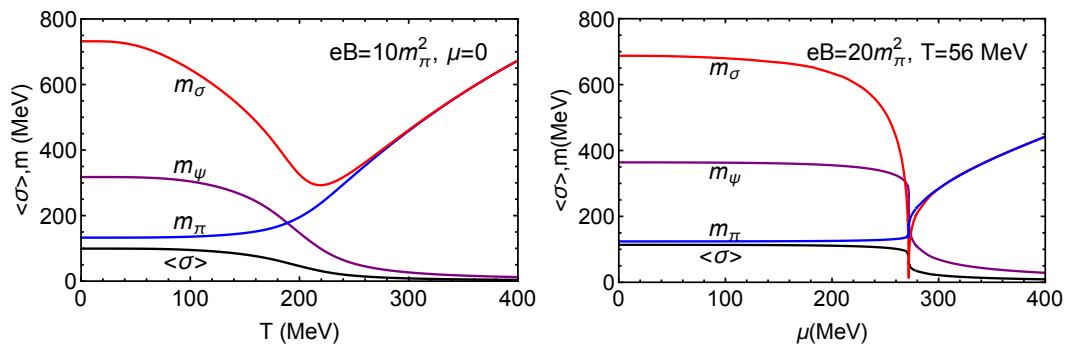


FIG. 2: Left: temperature dependence of meson screening masses m_σ , m_π , quark mass m_ψ , and the order parameter σ at $\mu = 0$ and $eB = 10m_\pi^2$. Right: chemical potential dependence of meson screening masses m_σ , m_π , quark mass m_ψ , and the order parameter σ at $T = 56$ MeV and $eB = 20m_\pi^2$.

The left panel of Fig. 2 shows the meson screening masses m_σ and m_π , the quark mass m_ψ , and the order parameter σ as functions of temperature at zero chemical potential under $eB = 10 m_\pi^2$. A common way to define the pseudo-critical temperature for the crossover is to locate the point where the order parameter varies most rapidly, giving $T_c = 196$ MeV for $eB = 10 m_\pi^2$. For stronger magnetic fields, $eB = 20$ and $30 m_\pi^2$, the pseudo-critical temperatures increase to $T_c = 212$ MeV and 222 MeV, respectively, confirming magnetic catalysis and agreeing with the results in [28]. At high temperatures, the sigma and pion masses become degenerate, while the order parameter drops sharply, reflecting the progressive restoration of chiral symmetry. The right panel of Fig. 2 displays the chemical potential

dependence of masses and the order parameter near the CEP for $eB = 20 m_\pi^2$. A very soft sigma mode emerges as its mass approaches zero at the CEP.

B. Spectral function at finite temperature

We now turn to the meson spectral functions. For comparison, we first present the spectral function at $T = 10$ MeV under zero density and magnetic field—conditions that closely mimic the vacuum. The result is consistent with that reported in [17]. However, since a different p_3 -regulator is used in this work compared to [17], it is necessary to first show the vacuum spectral function for reference. The pion spectral function displays a sharp peak near $\omega = 100$ MeV, which corresponds to the pion pole mass. In the truncation scheme used here, this pole mass is smaller than the corresponding screening mass. Such a discrepancy between pole and screening masses has also been reported in [17]. Although adopting a different set of UV parameters, as in [29, 35], could yield the correct pole mass, we retain the current parameter set because it produces the proper screening mass and thus ensures the correct threshold behavior in the spectral function. For energies above $\omega \geq 2m_\psi \approx 600$ MeV, an off-shell pion can decay into a quark–antiquark pair, which becomes kinematically allowed. This leads to a growth in the imaginary part of $\Gamma_\omega^{(2)}[\pi]$, and consequently enhances the pion spectral function for $\omega \geq 2m_\psi \approx 600$ MeV. On the other hand, the sigma spectral function shows a broad peak at $\omega = 280$ MeV, which arises from the opening of the decay channel $\sigma' \rightarrow \pi\pi$ near the threshold at $\omega = 275$ MeV, with ϕ' indicating an off-shell meson and ϕ an on-shell meson. The imaginary part of $\Gamma_\omega^{(2)}[\sigma]$ increases significantly around this energy, coinciding with a zero-crossing in the real part of $\Gamma_\omega^{(2)}[\sigma]$.

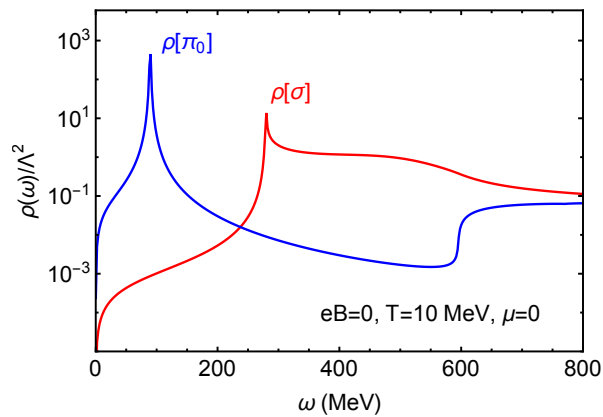


FIG. 3: Spectral function of sigma and pion at $T = 10$ MeV and vanishing density and magnetic field.

After turning on the magnetic field, π_0 and π_\pm are no longer degenerate. We show in Fig.4 the spectral functions of σ , π_0 , and π_+ at zero density under a magnetic field $eB = 10 m_\pi^2$ for various temperature. In the top panel, at $T = 10$ MeV, the π_0 spectral function (blue curve) has a sharp peak at $\omega = 82$ MeV, originating from the zero-crossing of the real part of $\Gamma_\omega^{(2)}[\pi_0]$. Compared to the $B = 0$ case in Fig.3, this peak shifts to a lower ω value, consistent with the decrease in the π_0 curvature mass as the magnetic field increases. The spectral function of the σ meson at $T = 10$ MeV and $eB = 10 m_\pi^2$ is shown as the red curve in the top panel. The peak shifts to a higher energy of $\omega \sim 504$ MeV compared to the $B = 0$ case in Fig. 3, which is consistent with the increase in the σ screening mass under stronger magnetic fields. In addition, the peak becomes broader relative to the $B = 0$ case. This broadening occurs because the decay channel $\sigma' \rightarrow \pi_0\pi_0$ opens around $\omega = 268$ MeV, leading to a rise in the imaginary part of $\Gamma_\omega^{(2)}[\sigma]$ before the real part undergoes zero-crossing. An enhancement emerges in the π_0 and σ spectral function around $\omega = 633$ MeV, due to the opening of the decay channel $\pi_0' \rightarrow \psi_0\bar{\psi}_0$ and $\sigma' \rightarrow \psi_0\bar{\psi}_0$, where ψ_0 denotes a u or d quark in the lowest Landau level and $\bar{\psi}_0$ the corresponding anti-quark. A similar increase occurs around $\omega = 960$ MeV, resulting from the decay $\pi_0' \rightarrow d_1\bar{d}_1$ and $\sigma' \rightarrow d_1\bar{d}_1$, which corresponds to an off-shell π_0 and σ decaying into a d-quark and an anti-d-quark pair in the first Landau level. It is important to note that, as indicated by the flow equations in (12), both π_0 and σ can only decay into quark-antiquark pairs occupying the same Landau level. Decay channels to mesons also contribute at high energy, which includes $\pi_0' \rightarrow \pi_0\sigma$ around $\omega = 864$ MeV, where an off-shell π_0 decays into an on-shell π_0 and a σ . Additionally, the decay channel $\sigma' \rightarrow \pi_+\pi_-$ contributes to the σ spectral function around $\omega = 894$ MeV.

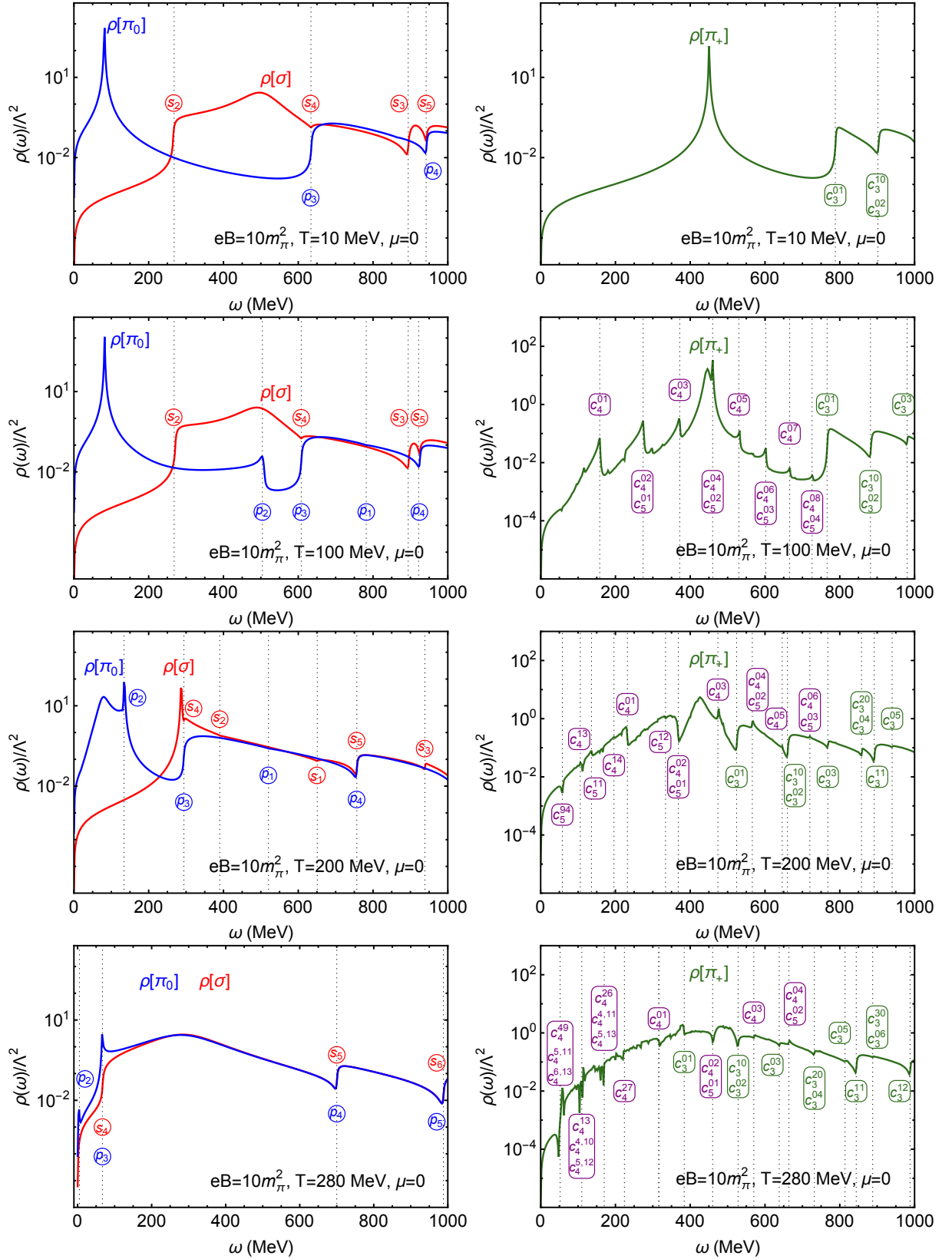


FIG. 4: Spectral functions of σ , π_0 (left panels) and π_+ (right panels) are shown versus external energy ω at $\mu = 0$ and magnetic field $eB = 10m_\pi^2$ for different temperature. Inserted annotations refer to the different processes affecting the spectral functions at the so indicated values of ω , $s_1 : \sigma' \rightarrow \sigma\sigma$, $s_2 : \sigma' \rightarrow \pi_0\pi_0$, $s_3 : \sigma' \rightarrow \pi_+\pi_-$, $s_4 : \sigma' \rightarrow \psi_0\psi_0$, $s_5 : \sigma' \rightarrow d_1\bar{d}_1$, $s_6 : \sigma' \rightarrow u_1\bar{u}_1$; $p_1 : \pi'_0 \rightarrow \pi_0\sigma$, $p_2 : \pi'_0\pi_0 \rightarrow \sigma$, $p_3 : \pi'_0 \rightarrow \psi_0\psi_0$, $p_4 : \pi'_0 \rightarrow d_1\bar{d}_1$, $p_5 : \pi'_0 \rightarrow u_1\bar{u}_1$; $c_1 : \pi'_+\sigma \rightarrow \pi_+$, $c_2 : \pi'_+\pi_- \rightarrow \sigma$, $c_3^{i,j} : \pi'_+ \rightarrow u_i\bar{d}_j$, $c_4^{i,j} : \pi'_+\bar{u}_i \rightarrow \bar{d}_j$, $c_5^{i,j} : \pi'_+d_i \rightarrow u_j$.

In the spectral function of π_+ at $T = 10$ MeV under a magnetic field of $eB = 10m_\pi^2$, represented by the green curve in top panel of Fig. 4, a sharp peak is observed at $\omega \sim 450$ MeV, corresponding to the mass of π_+ , which is consistent with $\sqrt{(m_{\pi_0}^{\text{pole}})^2 + eB}$. The spectral function is enhanced when decay into quark–antiquark pairs becomes kinematically allowed, specifically through channels of the form $\pi'_+ \rightarrow u_i \bar{d}_j$, where an off-shell charged pion decays into a u-quark in the i -th Landau level and a \bar{d} -quark in the j -th Landau level. According to the flow equation, a charged pion cannot decay into a quark and an antiquark both in the ground Landau level. However, decay into a pair both occupying the first Landau level is allowed; this occurs at $\omega = 1060$ MeV, though it lies outside the range shown in the figure. The dominant contribution at large energies comes from the channel $\pi'_+ \rightarrow u_0 \bar{d}_1$, in which the pion decays into a u-quark in the ground state and a \bar{d} -quark in the first Landau level. This occurs at $\omega = 788$ MeV. Similarly, at $\omega = 902$ MeV, both $\pi'_+ \rightarrow u_1 \bar{d}_0$ and $\pi'_+ \rightarrow u_0 \bar{d}_2$ can occur, resulting in further enhancement of the spectral function.

At $T = 100$ MeV, additional interesting structures emerge in the spectral functions due to thermal effects. The second row of Fig. 4 shows the spectral functions of the neutral mesons π_0 (blue curve) and σ (red curve). At this temperature, chiral symmetry remains broken, and the overall shapes of the π_0 and σ spectral functions are similar to those at $T = 10$ MeV. A new feature appears in the π_0 spectral function at $\omega = 511$ MeV, which is attributed to the annihilation process $\pi'_0 \pi_0 \rightarrow \sigma$, where an off-shell π_0 interacts with a thermally excited on-shell π_0 to produce an on-shell σ . As this process relies on thermal excitation, it occurs only at finite temperatures.

The π_+ spectral function at $T = 100$ MeV, presented as the green curve in the second row of Fig. 4, retains a general shape similar to that at $T = 10$ MeV, but exhibits a multi-peak structure. The main peak at $\omega = 446$ MeV, resulting from the zero-crossing of the real part of $\Gamma_\omega^{(2)}[\pi_+]$, corresponds to the pole mass of π_+ . As in the $T = 10$ MeV case, a series of enhancements occur at higher energies ($\omega > 766$ MeV) due to decays into quark–antiquark pairs across different Landau levels, i.e., $\pi'_+ \rightarrow u_i \bar{d}_j$. At lower energies, before these decay channels open, a multi-peak structure arises from processes involving annihilation with thermally excited quarks: specifically, $\pi'_+ \bar{u}_i \rightarrow \bar{d}_j$ and $\pi'_+ d_i \rightarrow u_j$. These processes occur only at finite temperature and become more significant as temperature increases. They induce minor changes in the real and imaginary parts of the spectral function, producing small peaks, as illustrated in Fig.6 in Appendix.A. Since these modifications are modest and do not alter the dominant structure, the corresponding peaks are relatively low in amplitude. For example, the peak annotated as c_4^{01} at $\omega = 158$ MeV corresponds to $\pi'_+ \bar{u}_0 \rightarrow \bar{d}_1$, where an off-shell π'_+ annihilates with a thermally excited \bar{u} -quark in the lowest Landau level to produce a \bar{d} -quark in the first Landau level. Similarly, c_4^{02} and c_5^{01} at the same energy denote the processes $\pi'_+ \bar{u}_0 \rightarrow \bar{d}_2$ and $\pi'_+ d_0 \rightarrow u_1$, respectively, which share the same threshold energy. A sequence of such processes occurs at various energies, as annotated in Fig. 4. Notably, all these involve a quark or antiquark in the lowest Landau level, since such excitations dominate the thermal bath. Processes involving higher Landau level quarks are suppressed and contribute minimally to the spectral function—though they may become more relevant at even higher temperatures.

At a temperature of $T = 200$ MeV and under a magnetic field of $eB = 10m_\pi^2$, as shown in the third row of Fig. 4, the σ spectral function (red curve) exhibits a peak at $\omega = 286$ MeV corresponding to the zero-crossing of the real part of $\Gamma_\omega^{(2)}[\sigma]$. Compared to the lower-temperature case, this sigma peak is sharper and narrower, indicating a more stable sigma meson near the crossover temperature. At this energy, decay into two pions or a quark–antiquark pair is not allowed. Just above the peak energy, decay into a ground-state quark–antiquark pair becomes possible, leading to a broadening of the peak. As the energy increases further, additional decay channels open, such as those into two σ mesons, two π_0 mesons, a pair of π_\pm mesons, and quark–antiquark pairs in the first Landau level, resulting in further enhancement of the spectral function. The π_0 spectral function (blue curve) shows a peak near $\omega = 82$ MeV due to the zero-crossing of the real part of $\Gamma_\omega^{(2)}[\pi_0]$, followed by another peak around $\omega = 134$ MeV. The latter originates from the process where an off-shell π'_0 annihilates with a thermally excited π_0 from the thermal medium to produce a σ meson. At higher energies, above the opening of the $\pi'_0 \rightarrow \psi_0 \psi_0$ decay channel near $\omega = 300$ MeV, the structure of the π_0 spectral function becomes qualitatively similar to that of the σ meson.

The π_+ spectral function at $T = 200$ MeV, represented by the green curve in the third row of Fig. 4, is overall lower and broader compared to the corresponding spectral function at $T = 100$ MeV. It is also broader than the σ and π_0 spectral functions at $T = 200$ MeV, suggesting that π_+ mesons are more readily dissolved in the thermal medium under a magnetic field. This behavior is associated with the various decay and annihilation channels available to the π_+ , as annotated in the boxes in the right panel. The main peak around 420 MeV arises from the zero-crossing of the real part of $\Gamma_\omega^{(2)}[\pi_+]$. Above $\omega = 524$ MeV, decays into $u_i \bar{d}_j$ quark pairs become allowed, each with a distinct threshold energy labeled as c_3^{ij} in the figure. At lower energies, the structure of the π_+ spectral function is influenced by annihilation processes between a π'_+ and thermally excited quarks or antiquarks. These annihilation channels contribute only weakly to the real and imaginary parts of $\Gamma_\omega^{(2)}[\pi_+]$, making the corresponding peaks less prominent or invisible once decay channels open. Since thermally excited quarks in high Landau levels are suppressed, the dominant contributions to annihilation come from quarks and antiquarks in the lowest Landau level. Thus, between

$\omega \approx 232$ MeV and $\omega \approx 720$ MeV, all relevant annihilation processes involve at least one quark or antiquark in the lowest Landau level. At even lower energies, where only annihilation channels associated with higher Landau levels are accessible, the spectral function displays an oscillatory-like structure. This arises from the dense spacing of threshold energies for annihilation processes involving quarks in higher Landau levels. A few such channels related to the first and higher Landau levels are annotated at low energies; many more contribute in this region.

At an even higher temperature of $T = 280$ MeV and for $eB = 10 m_\pi^2$, as shown in the last row of Fig. 4, the σ and π_0 spectral functions become nearly degenerate, except in the very soft region. The π_0 spectral function exhibits two additional peaks at $\omega = 4$ MeV and $\omega = 67$ MeV, originating from the processes $\pi'_0 \pi_0 \rightarrow \sigma$ and $\pi'_0 \rightarrow \psi_0 \psi_0$, respectively. For both σ and π_0 , the main peak around $\omega = 300$ MeV is very broad, suggesting that the mesons exist only as loosely bound states. At higher energies, decay channels into $\bar{d}d$ and $\bar{u}u$ pairs in the first Landau level open around 700 MeV and 1 GeV, respectively, leading to an enhancement in the spectral function. The π_+ spectral function exhibits significant broadening at $T = 280$ MeV and $eB = 10 m_\pi^2$ as shown in the last row of Fig. 4. This broadening causes its main peak around 490 MeV to merge with the small peaks from other processes and become nearly indistinguishable. Due to the reduced fermion mass and the higher thermal energy, a greater number of decay and annihilation channels—particularly those involving higher Landau levels—are present compared to the $T = 200$ MeV case. However, their individual contributions are minor.

C. Spectral function around the CEP

We further examine how meson spectral functions depend on the chemical potential in a magnetic field. Our analysis focuses on a temperature of $T = 56$ MeV and $eB = 20m_\pi^2$, corresponding to a horizontal line in the phase diagram across the critical endpoint (CEP). This choice allows us to study behavior near the CEP while maintaining significant thermal effects. We did not choose $eB = 10m_\pi^2$ because its CEP occurs at a very low temperature ($T = 25$ MeV), where thermal excitations are negligible. Nor did we choose $eB = 30m_\pi^2$, as the thresholds for key annihilation and decay channels would lie beyond our energy range of interest.

Over a wide range of chemical potentials, the spectral functions remain largely unchanged, which is consistent with the Silver Blaze property [36]. At $\mu = 200$ MeV, the neutral meson spectral functions in the top left panel of Fig. 5 resemble those at $\mu = 0$ and $T = 100$ MeV in Fig. 4, except that the decay channel into quark-antiquark pairs in the first Landau level is absent here. Due to the stronger magnetic field, the threshold for this channel exceeds 1 GeV and thus lies outside the energy range shown. As the critical endpoint is approached, however, significant changes emerge, particularly in the sigma spectral function. At $\mu = 270$ MeV, the sigma peak shifts to lower energy and narrows, signaling the formation of a more stable sigma meson near the CEP. Nevertheless, a discrepancy persists between the curvature mass and the pole mass: while the peak lies around $\omega = 450$ MeV, the threshold for the decay $\sigma' \rightarrow \sigma\sigma$ has already dropped to about 500 MeV. At the critical endpoint ($\mu = 273.7$ MeV), the sigma meson becomes a stable soft mode with a sharp peak near $\omega = 20$ MeV. In contrast, the $\sigma' \rightarrow \sigma\sigma$ threshold determined by the curvature mass—lags behind. This behavior stems from the extreme sensitivity of the pole mass to higher-order derivatives of the effective potential, combined with the rapid variation of the sigma curvature mass near the CEP. Upon further increasing the chemical potential, the sigma and pion spectral functions become degenerate, similar to the high-temperature case. A key difference, however, is that the spectral functions now display sharp peaks rather than broad resonances, indicating the emergence of stable dynamical quasi-particles.

The π_+ spectral function, shown in the right column of Fig. 4, also exhibits a multi-peak structure, with distinct features compared to the neutral mesons. While the neutral meson spectral functions remain nearly identical at $\mu = 200$ MeV and $\mu = 0$, the π_+ spectral function shows clear differences when compared to Fig. 7. At $\mu = 200$ MeV, the multi-peak structure is dominated by annihilation processes of the type $\pi'_+ d_i \rightarrow u_j$, labeled as c_5^{ij} . In contrast, contributions from $\pi'_+ \bar{u}_i \rightarrow \bar{d}_j$ (annotated as \bar{c}_4^{ij}) are negligible. This asymmetry arises because, at finite chemical potential, the medium is populated mainly by thermally excited quarks, while antiquarks are highly suppressed. As a result, with increasing chemical potential, processes like $\pi'_+ d_i \rightarrow u_j$ are enhanced, leading to larger and more prominent peaks; while those involving antiquarks are further suppressed, becoming weaker or even invisible. This effect can be seen, for example, by comparing the magnitudes of the c_4^{01} and c_5^{01} peaks in the π_+ spectral function at $\mu = 200$ MeV. Additionally, the peak labeled c_5^{11} grows with increasing chemical potential, reflecting the enhanced probability of such processes in a high-density environment. As μ rises, the quark mass decreases, lowering the energy threshold for the decay channel $\pi'_+ \rightarrow u_i \bar{d}_j$ and enabling contributions from higher Landau levels, as seen at $\mu = 273.7$ MeV and $\mu = 450$ MeV. Near the critical point, the sigma meson becomes soft, emerging as the lightest degree of freedom and the dominant thermal excitation in the medium. This gives rise to processes such as $\pi'_+ \sigma \rightarrow \pi_+$, which enhance and broaden the spectral function around $\omega = 400$ MeV. Unlike the neutral mesons, whose spectral functions develop sharp peaks at high density, the charged pion is a broad resonance due to the multitude of enhanced annihilation and decay channels available in this regime.

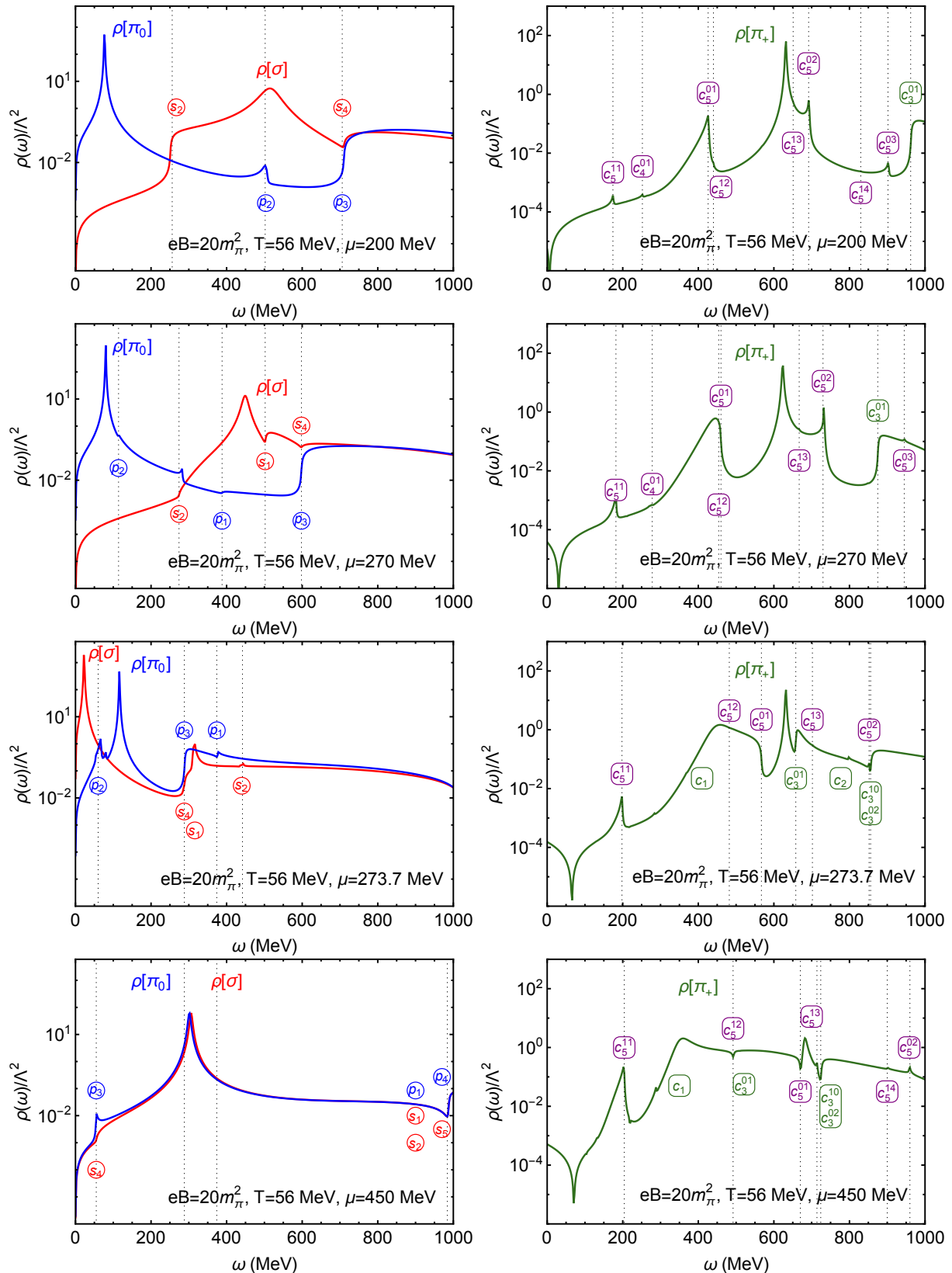


FIG. 5: Spectral functions of σ , π_0 (left panel) and π_+ (right panel) are shown versus external energy ω at $T = 56\text{MeV}$ and magnetic field $eB = 20m_\pi^2$ for various chemical potential μ . Inserted annotations refer to the different processes affecting the spectral functions at the so indicated values of ω , $s_1 : \sigma' \rightarrow \sigma\sigma$, $s_2 : \sigma' \rightarrow \pi_0\pi_0$, $s_3 : \sigma' \rightarrow \pi_+\pi_-$, $s_4 : \sigma' \rightarrow \psi_0\psi_0$, $s_5 : \sigma' \rightarrow d_1\bar{d}_1$, $s_6 : \sigma' \rightarrow u_1\bar{u}_1$; $p_1 : \pi'_0 \rightarrow \pi_0\sigma$, $p_2 : \pi'_0\pi_0 \rightarrow \sigma$, $p_3 : \pi'_0 \rightarrow \psi_0\psi_0$, $p_4 : \pi'_0 \rightarrow d_1\bar{d}_1$, $p_5 : \pi'_0 \rightarrow u_1\bar{u}_1$; $c_1 : \pi'_+\sigma \rightarrow \pi_+$, $c_2 : \pi'_+\pi_- \rightarrow \sigma$, $c_3^{ij} : \pi'_+ \rightarrow u_i\bar{d}_j$, $c_4^{ij} : \pi'_+\bar{u}_i \rightarrow \bar{d}_j$, $c_5^{ij} : \pi'_+d_i \rightarrow u_j$.

IV. SUMMARY

Although the mass spectrum of mesons in a magnetic field has been extensively studied, their dynamical properties in a magnetized medium remain relatively unexplored. In this work, we analyze the spectral functions of neutral and charged mesons at finite temperature and density under an external magnetic field, employing the two-flavor quark-meson model within the functional renormalization group (FRG) approach.

A key step in our analysis is the proper treatment of momentum relations at vertices for charged particles in the magnetic field. Based on this, we derive the flow equations for two-point functions of both neutral and charged mesons. The flow equation for the effective potential is solved using both the Taylor expansion around a fixed point and the grid method, with the two approaches yielding consistent results. Derivatives of the effective potential obtained during its flow evolution serve as inputs for integrating the flow equations of the two-point functions. Spectral functions are subsequently extracted via analytical continuation from Euclidean to Minkowski space.

These spectral functions offer crucial insights into the dynamical properties of mesons in a magnetized medium. They reveal how meson masses evolve during the chiral phase transition at finite temperature and density, with the σ spectral function notably exhibiting a soft mode near the critical endpoint. The momentum relations at interaction vertices further elucidate the underlying mechanisms: while σ and π_0 couple only to quark-antiquark pairs within the same Landau level, π_+ can couple to $u\bar{d}$ pairs across arbitrary Landau levels. This fundamental difference in coupling patterns leads to distinctly structured spectral functions for neutral and charged mesons under magnetic fields. Our results demonstrate that the spectral functions of σ and π_0 mesons develop new features due to decay channels involving quark-antiquark pairs occupying different Landau levels. In contrast, the charged pion spectral function displays a characteristic multi-peak structure at finite temperatures, originating from the multiple annihilation and decay channels unique to π_+ in a magnetic environment. This multi-peak pattern becomes more pronounced in a finite-density medium, where the π_+ meson forms a broad resonance at lower temperatures and densities compared to neutral mesons.

This multi-peak feature is expected to be universal for charged mesons under magnetic fields, suggesting the presence of numerous quasi-particle modes in the magnetized medium. This finding has significant implications for understanding transport properties in magnetized fluids.

Acknowledgments

We are grateful to Yangyang Tan, Shijun Mao, Shi Yin and Weijie Fu for fruitful discussions. The work is supported by NSFC grant Nos. 12005112 (Zy.W.).

Appendix A: Real and imaginary part of two-point function

To facilitate the interpretation of the structures observed in the spectral functions, we present the corresponding real and imaginary parts of the two-point functions. In Fig. 6, we show the real and imaginary parts of the two-point functions for σ , π_0 , and π_+ mesons at $T = 100$ MeV, $\mu = 0$, and $eB = 10 m_\pi^2$, corresponding to the spectral functions displayed in Fig. 4.

The real part of the sigma 2-point function exhibits a zero-crossing at $\omega \approx 484$ MeV. However, this does not correspond to a stable sigma state, as the imaginary part becomes non-zero already for $\omega \geq 2m_{\pi_0} \approx 270$ MeV, due to the decay of a sigma meson into two neutral pions. At $\omega \geq 2m_\psi \approx 608$ MeV, the decay into a quark-antiquark pair in the lowest Landau level also contributes to the imaginary part. Furthermore, the decay channel $\sigma' \rightarrow \pi_+\pi_-$, involving charged pions in the lowest Landau level, opens at $\omega \approx 894$ MeV. Since the sigma meson couples only to quark-antiquark pairs of the same flavor and same Landau level, the decay $\sigma' \rightarrow d_1\bar{d}_1$ becomes possible at $\omega \approx 922$ MeV, where both the d -quark and \bar{d} -antiquark reside in the first Landau level.

The real part of the π_0 2-point function shows a zero-crossing at $\omega \approx 90$ MeV, leading to a pronounced peak in the spectral function (Fig. 4), as the imaginary part remains negligible until $\omega \approx 504$ MeV, where the process $\pi_0'\pi_0 \rightarrow \sigma$ sets in. A small enhancement in both the real and imaginary parts appears for $\omega \geq m_\sigma + m_{\pi_0} \approx 782$ MeV, due to the decay into a sigma and a neutral pion. The decay into a quark-antiquark pair in the lowest Landau level contributes at $\omega \approx 608$ MeV, and the channel $\pi_0' \rightarrow d_1\bar{d}_1$ opens at $\omega \approx 922$ MeV, analogous to the sigma case.

The lower two panels of Fig. 6 show the real and imaginary parts of the π_+ 2-point function. The real part displays a zero-crossing at $\omega \approx 446$ MeV, corresponding to a sharp peak in the spectral function (Fig. 4), since the imaginary part remains nearly zero until the first decay channel opens at $\omega \approx 766$ MeV. The dominant structures in the two-point function arise from the decay channels $\pi_+' \rightarrow u_i\bar{d}_j$, denoted by c_3^{ij} , where the π_+ meson decays into a u -quark in the i -th Landau level and a \bar{d} -antiquark in the j -th Landau level. Because the π_+ can couple to $u\bar{d}$

pairs across arbitrary Landau levels (except when both are in the lowest level), the first decay channel $u_0\bar{d}_1$ opens at 766 MeV, followed by $u_1\bar{d}_0$ and $u_0\bar{d}_2$ at 882 MeV, and $u_0\bar{d}_3$ at 980 MeV. Since $u_1\bar{d}_0$ and $u_0\bar{d}_2$ contribute at the same threshold energy, their combined effect produces a change in the real and imaginary parts approximately twice as large as that from $u_0\bar{d}_1$ at 766 MeV.

To clarify the smaller variations below the decay threshold at $\omega \approx 766$ MeV, the imaginary part in the lower right panel is magnified by a factor of 10. The ability of π_+ to couple to $u\bar{d}$ pairs at arbitrary Landau levels enables a variety of annihilation processes, in which an off-shell π'_+ combines with a thermally excited \bar{u} or d quark to produce an on-shell \bar{d} or u quark in the magnetized thermal medium. These annihilation processes generate a sequence of small peaks in the real and imaginary parts of the two-point function, which in turn give rise to the multi-peak structure observed in the π_+ spectral function in Fig. 4.

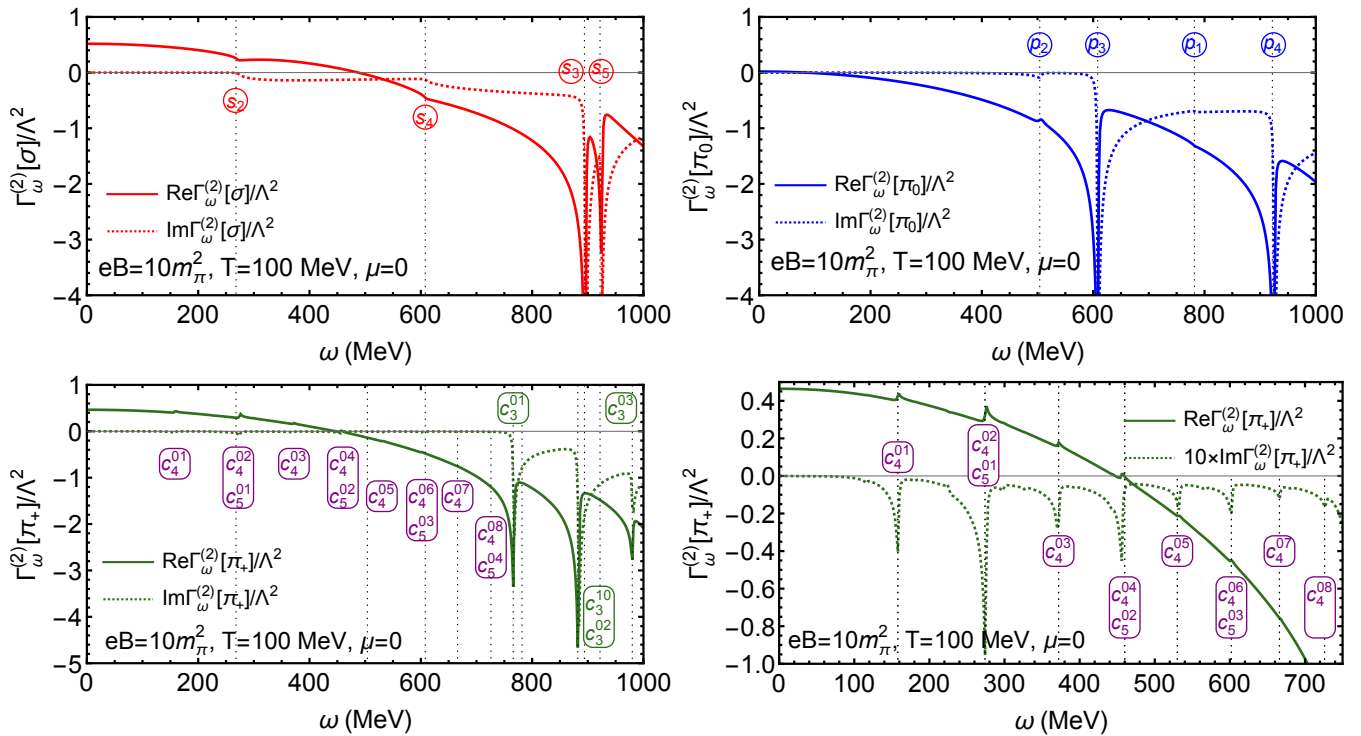


FIG. 6: Real part and imaginary part of σ , π_0 (upper two figures) and π_+ two-point functions (lower two figures) are shown versus external energy ω at $T = 100\text{MeV}$, $\mu = 0$ and magnetic field $eB = 10m_\pi^2$. Inserted annotations refer to the different processes affecting the spectral functions at the so indicated values of ω , $s_1 : \sigma' \rightarrow \sigma\sigma$, $s_2 : \sigma' \rightarrow \pi_0\pi_0$, $s_3 : \sigma' \rightarrow \pi_+\pi_-$, $s_4 : \sigma' \rightarrow \psi_0\bar{\psi}_0$, $s_5 : \sigma' \rightarrow d_1\bar{d}_1$, $s_6 : \sigma' \rightarrow u_1\bar{u}_1$; $p_1 : \pi'_0 \rightarrow \pi_0\sigma$, $p_2 : \pi'_0\pi_0 \rightarrow \sigma$, $p_3 : \pi'_0 \rightarrow \psi_0\bar{\psi}_0$, $p_4 : \pi'_0 \rightarrow d_1\bar{d}_1$, $p_5 : \pi'_0 \rightarrow u_1\bar{u}_1$; $c_1 : \pi'_+\sigma \rightarrow \pi_+$, $c_2 : \pi'_+\pi_- \rightarrow \sigma$, $c_3^{ij} : \pi'_+ \rightarrow u_i\bar{d}_j$, $c_4^{ij} : \pi'_+\bar{u}_i \rightarrow \bar{d}_j$, $c_5^{ij} : \pi'_+d_i \rightarrow u_j$.

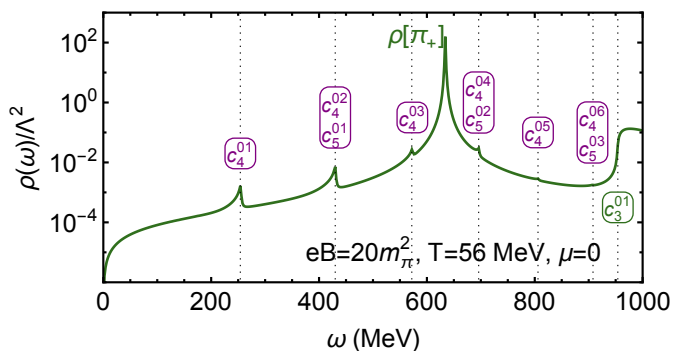


FIG. 7: Spectral function of π_+ at $T = 56\text{MeV}$, $\mu = 0$ and magnetic field $eB = 20m_\pi^2$. Inserted annotations refer to the different processes, $c_3^{ij} : \pi'_+ \rightarrow u_i\bar{d}_j$, $c_4^{ij} : \pi'_+\bar{u}_i \rightarrow \bar{d}_j$, $c_5^{ij} : \pi'_+d_i \rightarrow u_j$.

We further provide the π_+ spectral function at $T = 56$ MeV, $\mu = 0$, and $eB = 20 m_\pi^2$ in the appendix. This comparison is made with the corresponding spectral function at $\mu = 200$ MeV shown in the top panel of Fig. 5. At vanishing chemical potential, the annihilation processes $\pi'_+ \bar{u}_i \rightarrow \bar{d}_j$ and $\pi +' d_i \rightarrow u_j$ contribute equally. In contrast, at $\mu = 200$ MeV, the channel $\pi +' d_i \rightarrow u_j$ is noticeably enhanced, while $\pi'_+ \bar{u}_i \rightarrow \bar{d}_j$ becomes highly suppressed.

Appendix B: threshold function

With the boson and fermion occupation numbers and their derivatives,

$$\begin{aligned} n_B(x) &= \frac{1}{e^{x/T} - 1}, & n_F(x) &= \frac{1}{e^{x/T} + 1}, \\ n'_B(x) &= \frac{dn_B(x)}{dx}, & n'_F(x) &= \frac{dn_F(x)}{dx}, \end{aligned} \quad (\text{B1})$$

the threshold functions $I_\phi^{(1)T}$ and $I_f^{(1)T}$ in the flow equation for effective potential and $I_\phi^{(2)T}$ with four-line vertices are explicitly expressed as

$$\begin{aligned} I_\phi^{(1)T}(E_\phi) &= T \sum_{q_0} \frac{1}{(q_0^2 + E_\phi^2)} = \frac{1 + 2n_B(E_\phi)}{2E_\phi}, \\ I_f^{(1)T}(E_f) &= T \sum_{q_0} \frac{1}{((q_0 - i\mu)^2 + E_f^2)} = \frac{1 - n_F(E_f - \mu) - n_F(E_f + \mu)}{2E_f}, \\ I_\alpha^{(2)T}(E_\alpha) &= T \sum_{q_0} \frac{1}{(q_0^2 + E_\alpha^2)^2} = \frac{1}{4} \left(\frac{1 + 2n_B(E_\alpha)}{E_\alpha^3} - \frac{2n'_B(E_\alpha)}{E_\alpha^2} \right). \end{aligned} \quad (\text{B2})$$

After a straightforward but tedious calculation, the threshold function $L_{\phi_i \phi_j}(p_0)$ for meson loops with three-line vertices can be written as

$$\begin{aligned} J_{\alpha\alpha}^T &= T \sum_{q_0} \frac{1}{(q_0^2 + E_\alpha^2)^2 ((q_0 + p_0)^2 + E_\alpha^2)} \\ &= \frac{12E_\alpha^2 + p_0^2}{4E_\alpha^3 (4E_\alpha^2 + p_0^2)^2} (1 + 2n_B(E_\alpha)) - \frac{1}{2E_\alpha^2 (4E_\alpha^2 + p_0^2)} n'_B(E_\alpha), \\ J_{\alpha\beta}^T &= T \sum_{q_0} \frac{1}{(q_0^2 + E_\alpha^2)^2 ((q_0 + p_0)^2 + E_\beta^2)} \\ &= \frac{(E_\alpha^2 + E_\beta^2 - (2E_\alpha - ip_0)^2)}{4E_\alpha^3 (E_\beta^2 - (E_\alpha - ip_0)^2)^2} (1 + n_B(E_\alpha)) + \frac{(E_\alpha^2 + E_\beta^2 - (2E_\alpha + ip_0)^2)}{4E_\alpha^3 (E_\beta^2 - (E_\alpha + ip_0)^2)^2} n_B(E_\alpha) \\ &\quad + \frac{n'_B(E_\alpha)}{4E_\alpha^2 ((E_\alpha - ip_0)^2 - E_\beta^2)} + \frac{n'_B(E_\alpha)}{4E_\alpha^2 ((E_\alpha + ip_0)^2 - E_\beta^2)} \\ &\quad + \frac{1}{2E_\beta (E_\alpha^2 - (E_\beta + ip_0)^2)^2} (1 + n_B(E_\beta)) + \frac{1}{2E_\beta (E_\alpha^2 - (E_\beta - ip_0)^2)^2} n_B(E_\beta). \end{aligned} \quad (\text{B3})$$

For fermion loops, we divide $J_{ff}^{\sigma T}(p_0, \mu)$ into two terms for convenience,

$$\begin{aligned} J_{ff}^{\sigma T}(p_0, \mu) &= J_f^{(0)T}(p_0, \mu) + 4m^2 J_f^{(1)T}(p_0, \mu), \\ J_{ff}^{\pi_0 T}(p_0, \mu) &= J_f^{(0)T}(p_0, \mu). \end{aligned} \quad (\text{B4})$$

Threshold functions $J_{ff}^{(0,1)T}(p_0, \mu)$ encoding the Matsubata sum of loops composed by same flavor of quark are given by

$$\begin{aligned}
J_{ff}^{(0)T}(p_0, \mu) &= \frac{1}{2}T \sum_{q_0} \frac{-E_f^2 - (q_0 - i\mu)(q_0 + 2p_0 - i\mu)}{((q_0 - i\mu)^2 + E_f^2)((q_0 + p_0 - i\mu)^2 + E_f^2)} + \{\mu \leftrightarrow -\mu\} \\
&= \frac{(4E_f^2 - p_0^2)}{E_f(4E_f^2 + p_0^2)}(1 - n_F(E_f - \mu) - n_F(E_f + \mu)) + \frac{1}{4E_f^2 + p_0^2}(n'_F(E_f - \mu) + n'_F(E_f + \mu)), \\
J_f^{(1)T}(p_0, \mu) &= \frac{1}{2}T \sum_{q_0} \frac{1}{((q_0 - i\mu)^2 + E_f^2)((q_0 + p_0 - i\mu)^2 + E_f^2)} + \{\mu \leftrightarrow -\mu\} \\
&= -\frac{(12E_f^2 + p_0^2)}{4E_f^3(4E_f^2 + p_0^2)}(1 - n_F(E_f - \mu) - n_F(E_f + \mu)) - \frac{1}{4E_f^2(4E_f^2 + p_0^2)}(n'_F(E_f - \mu) + n'_F(E_f + \mu)).
\end{aligned}$$

Threshold function $J_{du,mn}^{(0,1)}$ with respect to the loop composed by a u-quark and a d-quark is given by

$$\begin{aligned}
J_{du,mn}^{(0)}(p_0, \mu) &= T \sum_{q_0} \frac{-(q_0 - i\mu)(q_0 + 2p_0 - i\mu) - E_{d,m}^2}{[(q_0 + p_0 - i\mu)^2 + E_{u,n}^2][(q_0 - i\mu)^2 + E_{d,m}^2]} \\
&= -\frac{(E_{d,m}^2 - E_{u,n}^2 + p_0^2)}{2E_{d,m}(E_{u,n}^2 - (E_{d,m} - ip_0)^2)}(1 - n_F(E_{d,m} + \mu)) + \frac{(E_{d,m}^2 - E_{u,n}^2 + p_0^2)}{2E_{d,m}(E_{u,n}^2 - (E_{d,m} + ip_0)^2)}n_F(E_{d,m} - \mu) \\
&\quad - \frac{(-E_{d,m}^2 + E_{u,n}^2 + p_0^2)}{2E_{u,n}(E_{d,m}^2 - (E_{u,n} + ip_0)^2)}(1 - n_F(E_{u,n} + \mu)) + \frac{(-E_{d,m}^2 + E_{u,n}^2 + p_0^2)}{2E_{u,n}(E_{d,m}^2 - (E_{u,n} - ip_0)^2)}n_F(E_{u,n} - \mu) \\
&\quad + \frac{ip_0}{2E_{d,m}(E_{u,n}^2 - (E_{d,m} - ip_0)^2)}n'_F(E_{d,m} + \mu) - \frac{ip_0}{2E_{d,m}(E_{u,n}^2 - (E_{d,m} + ip_0)^2)}n'_F(E_{d,m} - \mu), \\
J_{du,mn}^{(1)}(p_0, \mu) &= T \sum_{q_0} \frac{1}{[(q_0 + p_0 - i\mu)^2 + E_{u,n}^2][(q_0 - i\mu)^2 + E_{d,m}^2]} \\
&= -\frac{(E_{d,m}^2 + E_{u,n}^2 - (2E_{d,m} - ip_0)^2)}{4E_{d,m}^3(E_{u,n}^2 - (E_{d,m} - ip_0)^2)}(1 - n_F(E_{d,m} + \mu)) + \frac{(E_{d,m}^2 + E_{u,n}^2 - (2E_{d,m} + ip_0)^2)}{4E_{d,m}^3(E_{u,n}^2 - (E_{d,m} + ip_0)^2)}n_F(E_{d,m} - \mu) \\
&\quad - \frac{1 - n_F(E_{u,n} + \mu)}{2E_{u,n}(E_{d,m}^2 - (E_{u,n} + ip_0)^2)} + \frac{n_F(E_{u,n} - \mu)}{2E_{u,n}(E_{d,m}^2 - (E_{u,n} - ip_0)^2)} \\
&\quad + \frac{n'_F(E_{d,m} + \mu)}{4E_{d,m}^2(-E_{u,n}^2 + (E_{d,m} - ip_0)^2)} + \frac{n'_F(E_{d,m} - \mu)}{4E_{d,m}^2(-E_{u,n}^2 + (E_{d,m} + ip_0)^2)}. \tag{B5}
\end{aligned}$$

Likewise, with the regulator rest of the other propagator, one has $J_{ud,nm}^{(0,1)}$ from the above by exchanging $E_{u,n} \leftrightarrow E_{d,m}$,

$$\begin{aligned}
J_{ud,nm}^{(0)}(p_0, \mu) &= T \sum_{q_0} \frac{-(q_0 - i\mu)(q_0 + 2p_0 - i\mu) - E_{u,n}^2}{[(q_0 + p_0 - i\mu)^2 + E_{d,m}^2][(q_0 - i\mu)^2 + E_{u,n}^2]} = J_{du,mn}^0(p_0, \mu)\{E_{u,n} \leftrightarrow E_{d,m}\}, \\
J_{ud,nm}^{(1)}(p_0, \mu) &= T \sum_{q_0} \frac{1}{[(q_0 + p_0 - i\mu)^2 + E_{d,m}^2][(q_0 - i\mu)^2 + E_{u,n}^2]} = J_{du,mn}^1(p_0, \mu)\{E_{u,n} \leftrightarrow E_{d,m}\}. \tag{B6}
\end{aligned}$$

Appendix C: Meson loop and quark loop with different electric charge

Translating from the Feynman digram, the meson loop composed by σ and π_+ with two three-line vertex is

$$\begin{aligned}
\text{M-Loop} &= (\Gamma_{\sigma\pi\pi}^{(3)})^2 \int_{r,r'} \phi_{np}(r')G_{\pi_+}(r, r')G_{\sigma}(r', r)\phi_{np}^*(r) \\
&= (\Gamma_{\sigma\pi\pi}^{(3)})^2 \int d^4r d^4r' e^{-ip_0t' + ip_3z'} \Psi_{np1}(\vec{r}'_{\perp}) e^{ip_0t - ip_3z} \Psi_{np1}^*(\vec{r}_{\perp}) \\
&\quad \times \int \frac{d^4q d^4k}{((2\pi)^4)^2} e^{-i(k-q)\cdot(r-r')} e^{-is_{\perp} \frac{(x-x')(y+y')}{2t^2}} G_{\pi_+}(k)G_{\sigma}(q), \tag{C1}
\end{aligned}$$

where $r = (t, x, y, x)$, $r' = (t', x', y', x')$. $G_{\pi_+}(r, r')$ and $G_{\sigma}(r', r)$ are propagators of π_+ and σ in coordinate space respectively, they are the Fourier transformation of propagators in momentum space. For π_+ , it is given by (5). The integral over t and z yields the momentum conservation in the zeroth and third component, while the integral over \vec{r}_{\perp} and \vec{r}'_{\perp} is nontrivial, and can be carried out using the following expression,

$$\int_{-\infty}^{+\infty} e^{ixy} e^{-x^2/2} H_n(x) dx = \sqrt{2\pi} i^n e^{-y^2/2} H_n(y). \quad (C2)$$

Considering that we have set the external line to be in the ground state $n = 0$, the integral over coordinates in (C1) yields

$$\text{M-Loop} = (\Gamma_{\sigma\pi\pi}^{(3)})^2 4l^2 \sum_{m=0}^{\infty} \int \frac{d^2 k_{\perp}}{(2\pi)^2} \frac{d^4 q}{(2\pi)^4} e^{-2k_{\perp}^2 l^2} e^{-q_{\perp} l^2} e^{-2l^2 \vec{q}_{\perp} \cdot \vec{k}_{\perp}} \frac{1}{q_0^2 - \vec{q}^2 - m_{\sigma}^2} \frac{1}{(q_0 + p_0)^2 - (2m+1)|eB| - q_3^2 - m_{\pi}^2} \frac{(-1)^m L_m(2k_{\perp}^2 l^2)}{(C3)}$$

The integral over \vec{k}_{\perp} can then be done using

$$\int_0^{\infty} x e^{-x^2} L_n(x^2) J_0(xy) = \frac{2^{-2n-1}}{n!} y^{2n} e^{-\frac{1}{4}y^2}. \quad (C4)$$

Finally, one arrives at

$$\text{M-Loop} = (\Gamma_{\sigma\pi\pi}^{(3)})^2 \sum_{m=0}^{\infty} \int \frac{d^4 q}{(2\pi)^4} \frac{1}{q_0^2 - \vec{q}^2 - m_{\sigma}^2} \frac{1}{(q_0 + p_0)^2 - (2m+1)|eB| - q_3^2 - m_{\pi}^2} \frac{1}{m!} \left(\frac{l^2 q_{\perp}^2}{2}\right)^m e^{-\frac{1}{2}l^2 q_{\perp}^2}. \quad (C5)$$

One can then implement the Wick rotation and FRG modification by taking the replacement $p_3^2 \rightarrow p_3^2(1 + r_B)$. The flow equation is then derived by taking derivative respective to RG-scale k . Taking the limit $|eB| \rightarrow 0$, one can obviously find that the summation over Landau level becomes trivial. With $(2m+1)|eB|$ becoming \vec{q}_{\perp}^2 , the summation $\sum_{m=0}^{\infty} \frac{1}{m!} \left(\frac{l^2 q_{\perp}^2}{2}\right)^m = e^{\frac{1}{2}l^2 q_{\perp}^2}$ cancels with the other exponential in (C5). Then (C5) goes back to the expression without the background magnetic field.

The quark loop constructed by u quark and d quark also appears in the π_+ two-point function. The Schwinger phase of the u d quark cannot cancel out, thus one has to calculate the quark loop starting from the coordinate space. The quark propagator in the coordinate space can also be obtained by Fourier transformation (5) from the momentum space propagator (7). This fermion loop in the coordinate space is

$$\begin{aligned} \text{F-loop} &= \int_{r, r'} \text{Tr} \left[\phi_{np}(r') (\sqrt{2}ig\gamma_5) G_u(r, r') (\sqrt{2}ig\gamma_5) G_d(r', r) \phi_{np}^*(r) \right] \\ &= 2 \int d^4 r d^4 r' e^{-ip_0 t' + ip_3 z'} \Psi_{np_1}(\vec{r}'_{\perp}) e^{ip_0 t - ip_3 z} \Psi_{np_1}^*(\vec{r}_{\perp}) \times \int \frac{d^4 k}{(2\pi)^4} e^{-ik_0(t-t') + i\vec{k} \cdot (\vec{r} - \vec{r}')} e^{-is_{\perp}^u \frac{(x-x')(y+y')}{2l^2}} \\ &\quad \times \int \frac{d^4 q}{(2\pi)^4} e^{-iq_0(t-t) + i\vec{q} \cdot (\vec{r}' - \vec{r})} e^{-is_{\perp}^d \frac{(x'-x)(y+y')}{2l^2}} \times \text{tr}[G_u(k) i\gamma^5 G_d(q) i\gamma^5], \end{aligned} \quad (C6)$$

taking $l = 1/\sqrt{|eB|}$, then for u-quark $s_{\perp}^u = +1$, $l_u^2 = \frac{3}{2}l^2$, and for d-quark $s_{\perp}^d = -1$, $l_d^2 = 3l^2$. The integral over t, z gives momentum conservation in zeroth and third component of momentum, while the integral over \vec{r}_{\perp} and \vec{r}'_{\perp} gives

$$\int dx dx' \int dy dy' e^{i\vec{k}_{\perp} \cdot (\vec{r}_{\perp} - \vec{r}'_{\perp}) + i\vec{q}_{\perp} \cdot (\vec{r}'_{\perp} - \vec{r}_{\perp})} e^{-i \frac{(x-x')(y+y')}{2l^2}} \Psi_{np_1}(\vec{r}'_{\perp}) \Psi_{np_1}^*(\vec{r}_{\perp}) = 2\pi 2l^2 e^{-l^2(\vec{k}_{\perp} - \vec{q}_{\perp})^2}, \quad (C7)$$

where the external line $\Psi_{np_1}(\vec{r}'_{\perp})$ is given by (13), and for the external line, we take the lowest Landau level $n = 0$. After evaluating the Dirac trace, integrating k_0 and k_3 using the δ -function and analytically completing the integral over \vec{k}_{\perp} using

$$\int_0^{\infty} x^{\nu+1} e^{-\beta x^2} L_n^{\nu}(\alpha x^2) J_{\nu}(xy) dx = 2^{-\nu-1} \beta^{-\nu-n-1} (\beta - \alpha)^n y^{\nu} e^{-\frac{y^2}{4\beta}} L_n^{\nu} \left[\frac{\alpha y^2}{4\beta(\alpha - \beta)} \right], \quad (C8)$$

one finally arrives at

$$\begin{aligned} \text{F-loop} &= 4 \int \frac{d^4 q}{(2\pi)^4} \sum_{h, m=0}^{\infty} \frac{(-1)^m}{[(p_0 + q_0)^2 - 2h|q_u B| - (p_3 + q_3)^2 - m_u^2][q_0^2 - 2m|q_d B| - q_3^2 - m_d^2]} \frac{8}{5^h} \\ &\quad \times \left\{ (q_0(p_0 + q_0) - q_3(p_3 + q_3) - m_u m_d) \left[e^{-\frac{18}{5}q_{\perp}^2 l^2} \left(\frac{1}{5} L_h \left(-\frac{12}{5} q_{\perp}^2 l^2 \right) L_{m-1}(6q_{\perp}^2 l^2) - L_{h-1} \left(-\frac{12}{5} q_{\perp}^2 l^2 \right) L_m(6q_{\perp}^2 l^2) \right) \right] \right. \\ &\quad \left. - \frac{16}{5} q_{\perp}^2 e^{-\frac{18}{5}q_{\perp}^2 l^2} L_{h-1}^1 \left(-\frac{12}{5} q_{\perp}^2 l^2 \right) L_{m-1}^1(6q_{\perp}^2 l^2) \right\}. \end{aligned} \quad (C9)$$

The integral over perpendicular momentum \vec{q}_\perp can be performed analytically, giving two functions $Y_1(m, n)$ and $Y_2(m, n)$ defined in (19). Then we perform the Wick rotation to Euclidean space, consider the RG modification to the propagator and the chemical potential. The quark loop in the two point function becomes

$$2g^2 \tilde{\partial}_k \text{Tr}[G_u(i\gamma^5)G_d(i\gamma^5)] = 2g^2 N_c \left(J_{du}^{\pi+}(p_0, \mu) + J_{ud}^{\pi+}(-p_0, \mu) \right), \quad (\text{C10})$$

with the loop functions $J_{du}^{\pi+}$ and $J_{ud}^{\pi+}$ given by (18).

-
- [1] Wei-Tian Deng and Xu-Guang Huang. Event-by-event generation of electromagnetic fields in heavy-ion collisions. *Phys. Rev. C*, 85:044907, 2012.
- [2] V. Skokov, A. Illarionov, and V. Toneev. Estimate of the magnetic field strength in heavy-ion collisions. *Int.J.Mod.Phys.A*, 24:5925–5932, 2009.
- [3] Dario Grasso and Hector R. Rubinstein. Magnetic fields in the early universe. *Phys. Rept.*, 348:163–266, 2001.
- [4] V.P. Gusynin, V.A. Miransky, and I.A. Shovkovy. Dimensional reduction and dynamical chiral symmetry breaking by a magnetic field in $3 + 1$ dimensions. *Kiev-ITP-94-58E*, 1995.
- [5] V.P. Gusynin, V.A. Miransky, and I.A. Shovkovy. Dimensional reduction and catalysis of dynamical symmetry breaking by a magnetic field. *UCLA/95/TEP/26*, 1995.
- [6] F. Bruckmann, G. Endrodi, and T. G. Kovacs. Inverse magnetic catalysis and the polyakov loop. 03 2013.
- [7] Falk Bruckmann, Gergely Endrodi, and Tamas G. Kovacs. Inverse magnetic catalysis in qcd. 11 2013.
- [8] Jingyi Chao, Pengcheng Chu, and Mei Huang. Inverse magnetic catalysis induced by sphalerons. 05 2013.
- [9] Christoph P. Hofmann. Diamagnetic and paramagnetic phases in low-energy quantum chromodynamics. 03 2021.
- [10] V. D. Orlovsky and Yu. A. Simonov. Magnetic susceptibility in qcd. 05 2014.
- [11] Gergely Endrodi. Qcd equation of state at nonzero magnetic fields in the hadron resonance gas model. 01 2013.
- [12] Sh. Fayazbakhsh and N. Sadooghi. Anomalous magnetic moment of hot quarks, inverse magnetic catalysis and reentrance of chiral symmetry broken phase. *Phys. Rev.*, D90:105030, 2014.
- [13] G. S. Bali, F. Bruckmann, G. Endrodi, S. D. Katz, and A. Schafer. The qcd equation of state in background magnetic fields. 06 2014.
- [14] Kenji Fukushima, Dmitri E. Kharzeev, and Harmen J. Warringa. The chiral magnetic effect. *Phys.Rev.D*, 78:074033, 2008.
- [15] Dmitri E. Kharzeev, Larry D. McLerran, and Harmen J. Warringa. The effects of topological charge change in heavy ion collisions: "event by event p and cp violation". *Nucl.Phys.A*, 803:227–253, 2008.
- [16] D. E. Kharzeev, J. Liao, S. A. Voloshin, and G. Wang. Chiral magnetic and vortical effects in high-energy nuclear collisions — a status report. 11 2015.
- [17] Ralf-Arno Tripolt, Nils Strodthoff, Lorenz von Smekal, and Jochen Wambach. Spectral functions for the quark-meson model phase diagram from the functional renormalization group. *Phys. Rev. D*, 89:034010, 2014.
- [18] Jozef J. Dudek, Robert G. Edwards, Peng Guo, and Christopher E. Thomas. Toward the excited isoscalar meson spectrum from lattice qcd. *JLAB-THY-13-1786, TCDMATH 13-11*, 09 2013.
- [19] Martina Blank. Properties of quarks and mesons in the dyson-schwinger/bethe-salpeter approach. 06 2011.
- [20] N. Tetradis. The quark-meson model and the phase diagram of two-flavour qcd. *Nucl.Phys.*, A726:93–119, 2003.
- [21] Tina K. Herbst, Jan M. Pawłowski, and Bernd-Jochen Schaefer. On the phase structure and thermodynamics of qcd. *Phys. Rev. D*, 88:014007, 2013.
- [22] Wei jie Fu and Jan M. Pawłowski. On the relevance of matter and glue dynamics for baryon number fluctuations. *Phys. Rev. D*, 92:116006, 2015.
- [23] Janos Polonyi. Lectures on the functional renormalization group method. *Central Eur.J.Phys.*, 1:1–71, 2003.
- [24] Christof Wetterich. Exact evolution equation for the effective potential. *Phys. Lett. B*, 301:90–94, 1993.
- [25] Jan M. Pawłowski. Aspects of the functional renormalisation group. *Annals Phys.*, 322:2831–2915, 2007.
- [26] Holger Gies. Introduction to the functional RG and applications to gauge theories. *Lect. Notes Phys.*, 852:287–348, 2012.
- [27] Jens O. Andersen, William R. Naylor, and Anders Tranberg. Chiral and deconfinement transitions in a magnetic background using the functional renormalization group with the polyakov loop. 11 2013.
- [28] Kazuhiko Kamikado and Takuya Kanazawa. Chiral dynamics in a magnetic field from the functional renormalization group. *JHEP03(2014)009*, 12 2013.
- [29] Rui Wen, Shi Yin, Wei jie Fu, and Mei Huang. Functional renormalization group study of neutral and charged pion under magnetic fields in the quark-meson model. 06 2023.
- [30] Julian S. Schwinger. On gauge invariance and vacuum polarization. *Phys. Rev.*, 82:664–679, 1951.
- [31] Vladimir A. Miransky and Igor A. Shovkovy. Quantum field theory in a magnetic field: From quantum chromodynamics to graphene and dirac semimetals. *Physics Reports*, 576:1–209, 2015.
- [32] Jan M. Pawłowski and Fabian Rennecke. Higher order quark-mesonic scattering processes and the phase structure of qcd. 03 2014.
- [33] B. Stokic, B. Friman, and K. Redlich. The functional renormalization group and $o(4)$ scaling. *Eur.Phys.J.C*, 67:425–438, 2010.

- [34] Bernd-Jochen Schaefer and Jochen Wambach. The phase diagram of the quark-meson model. *Nucl.Phys.*, A757:479–492, 2005.
- [35] Ziyue Wang and Pengfei Zhuang. Meson spectral functions at finite temperature and isospin density with the functional renormalization group. *Phys. Rev. D*, 96(1):014006, 2017.
- [36] Thomas D . Cohen. Functional integrals for QCD at nonzero chemical potential and zero density. *Phys. Rev. Lett.*, 91:222001, 2003.